

Future Projections of Extreme Precipitation across Massachusetts: a Theory-Based Approach

Technical Documentation

**Scott Steinschneider
Nasser Najibi**

**Biological and Environmental Engineering
Cornell University
Ithaca, NY**

1. Introduction

Extreme precipitation poses a significant risk to infrastructure across the state of Massachusetts, and this risk is poised to increase with climate change. There is a vast body of literature showing that extreme precipitation is likely to intensify as the climate warms, both globally and in the Northeast US (Ali et al., 2018; Howarth et al., 2019). Therefore, it is critical that new design standards be determined for Massachusetts infrastructure that account for potential increases in extreme precipitation, so that communities are better able to mitigate the impacts of these extreme events over the next several decades. The purpose of this report is to identify observed and projected changes in extreme precipitation across Massachusetts, and to forward recommendations for how to adjust design storms to accommodate these changes.

To help determine how design storms may change in the future, it is instructive to focus on the different causal pathways in the climate system that can lead to these changes. The physical causes of future climate change can be classified as either thermodynamic or dynamic in nature (Emori and Brown, 2005; Seager et al., 2010). Thermodynamic climate changes relate directly to the increased surface warming of the Earth under human-induced greenhouse gas emissions. For extreme precipitation, thermodynamic change is driven by the increased moisture holding capacity of a warmer atmosphere. The Clausius-Clapeyron (C-C) equation determines the relationship between saturated water vapor pressure and air temperature and shows that the atmospheric moisture-holding capacity increases by $\sim 7\%$ per $^{\circ}\text{C}$ warming (Alduchov & Eskridge, 1996). If all other factors controlling precipitation intensity remain unchanged, it is often assumed that extreme precipitation will scale with temperature at the same C-C scaling rate (Allen & Ingram 2002; Allan & Soden, 2008). The reasoning is that under conditions that lead to extreme precipitation (i.e., near saturated atmospheric conditions; intense surface convergence and uplift), changes in atmospheric moisture content will translate directly to changes in precipitation amount. This type of thermodynamic climate change in extreme precipitation is consistent across theory, observations, and model projections (IPCC 2013; Pfahl et al., 2017), leading to high confidence in the future direction of change, albeit with residual uncertainty in its magnitude.

Dynamic climate changes in extreme precipitation are related to shifts in atmospheric circulation (e.g., jet stream dynamics, storm tracks) and are significantly more uncertain than thermodynamic change (Pfahl et al., 2017), leading to large uncertainties in projected precipitation patterns (Hawcroft et al., 2016; Shepherd, 2014; Woollings, 2010; Zappa et al., 2013). Dynamic changes arise within the non-linear dynamics of the coupled atmosphere-ocean system that can produce multi-decadal oscillations in regional precipitation with no well-defined periodicity (Liu, 2012; Han et al., 2014; Newman et al., 2016). This makes dynamic changes particularly difficult to distinguish from natural atmospheric variability unrelated to anthropogenic climate change (Shepherd, 2014; Deser et al., 2012), especially over shorter timeframes (30-50 years) relevant to water system planning (Hawkins and Sutton, 2011). Uncertainty in projections not attributable to differences in boundary forcing or internal variability are linked to errors in the underlying climate models (Knutti & Sedlacek, 2013). These errors are often driven by unresolved processes (Randall et al., 2003), which also have a large impact on projections of future large-scale atmospheric dynamics (Barnes and Polvani, 2013; van Niekerk et al., 2017). This type of dynamical error severely complicates attempts to bias correct GCM output because the bias will likely change over time (Maraun, et al. 2017).

Very detailed climate model experiments and analysis are required to attribute projected shifts in extreme precipitation to true dynamical climate change and separate it from climate model bias or internal variability. When such studies are beyond the scope and available resources of a climate change analysis, or when there is significant, irreducible uncertainty in the dynamic components of climate change, there is strong justification to focus only on the thermodynamic aspects of climate change for which there is more confidence (Pfahl et al., 2017). This is the approach taken in this report, which focuses on developing a better understanding of thermodynamic scaling of observed and projected extreme precipitation with warming over the state of Massachusetts.

There are multiple factors that can modulate extreme precipitation scaling over a specific region, yielding greater or lower scaling than the theoretical C-C rate of $\sim 7\%$ per $^{\circ}\text{C}$ (e.g., see Table 1 in Pumo et al., 2019). For instance, scaling rates can depend strongly on the resolution of precipitation data used in the analysis (daily vs. sub-daily; Visser et al., 2020). There is also strong evidence that extreme precipitation scales more closely with dew point temperature rather than air temperature, as the former better reflects changes in moisture available to drive changes in precipitation (Ali et al., 2018). In addition, scaling rates can vary depending on the modeling approach used to determine the scaling rate (see Martinkova & Kysely, 2020). Finally, scaling can vary significantly depending on whether precipitation events are separated by storm type (e.g., convective vs. stratiform) or weather regime (WR), the latter defined as reoccurring, large-scale patterns of atmospheric flow that influence weather over a region (Magan et al., 2020; Martinkova & Kysely, 2020).

This report assesses how extreme precipitation scales with dew point temperature, both in the observational record across the Northeast US and in a set of downscaled climate projections specific to the state of Massachusetts. Scaling rates are examined on a variety of temporal scales, including at the annual, seasonal, and daily levels, using a variety of different statistical methods to ensure the robustness of results. Scaling rates are also examined under different WRs for the Northeast US, to determine if background atmospheric dynamics influence observed thermodynamic scaling rates. All inferred scaling rates of extreme precipitation with warming are compared against the benchmark, theoretical C-C scaling rate of 7% per $^{\circ}\text{C}$. The overarching goal of these analyses is to determine an appropriate scaling rate that can be used to project thermodynamic changes in design storm events across the state of Massachusetts based on an ensemble of temperature projections across the state.

2. Data

2.1. Observational Data

Observed daily temperature and precipitation are collected across 93 weather stations in the Northeast US from the global summary of day (GSOD) dataset contained in the Integrated Surface Data (ISD) (<https://www.ncdc.noaa.gov/isd>) (Figure 1). We collected stations across the Northeast US, rather than only in Massachusetts, to ensure a sufficient dataset to explore thermodynamic scaling of extreme precipitation with warming. We selected the 93 ISD-GSOD stations using a three step process. First, we identified all the stations located in Connecticut, Delaware, District of Columbia, Maine, Maryland, Massachusetts, New Hampshire, New Jersey, New York, Pennsylvania, Rhode Island, and Vermont. Next, we flagged any year with more than 10% missing days across three variables (precipitation (P), air temperature (Ta), and dew point temperature (Td)) between March 1, 1948, and February 29, 2020 and labeled those years as incomplete.

Finally, we selected those stations that have at least 10 years of complete yearly records. The selected 93 stations have over 21 years of observations per site on average. The screening process was made relatively strict to ensure sufficient daily records at each station to manage sampling variability in the estimated relationship between extreme precipitation and dew point temperature.

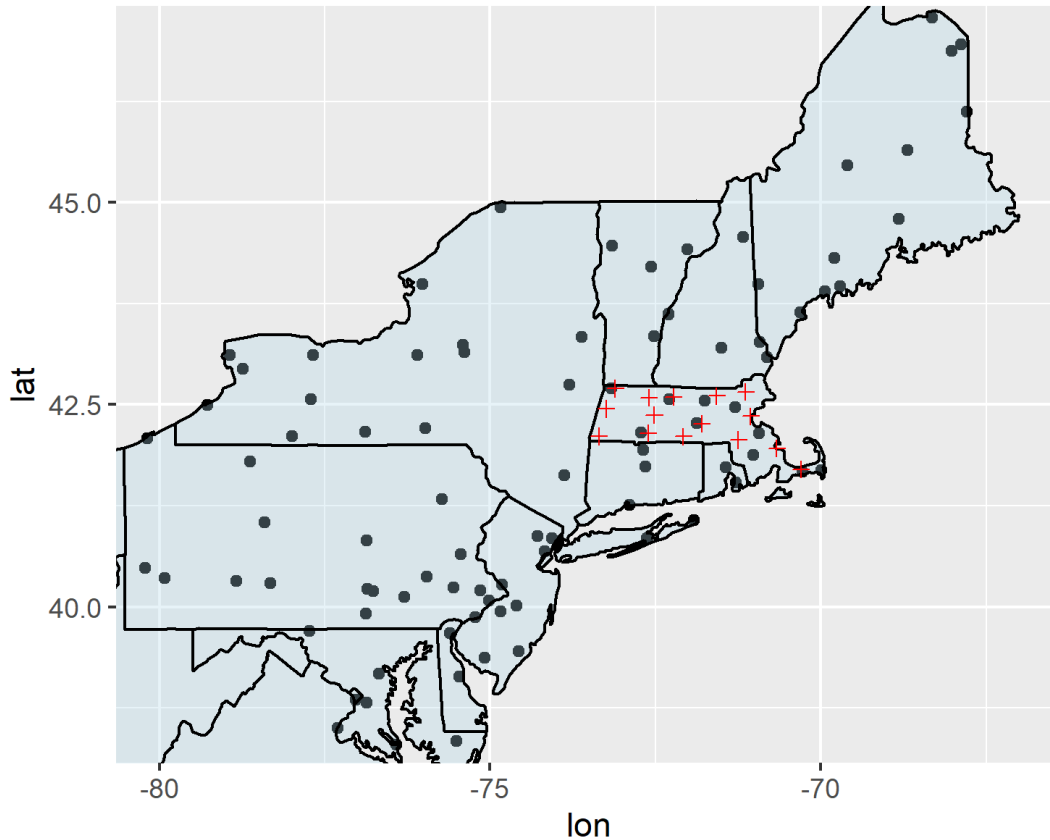


Figure 1. Map of observed ISD-GSOD stations (black) and locations of downscaled climate model projections (red).

We also obtained daily gridded ($2.5^\circ \times 2.5^\circ$) geopotential heights (GPH) [m] at the 500-hPa level from the National Centers for Environmental Prediction (NCEP)/National Center for Atmospheric Research (NCAR) reanalysis (NCEP/NCAR Reanalysis 1) dataset (Kalnay et al., 1996) between March 1, 1948, and February 29, 2020 (72 years). The gridded data were then extracted for the region between 30°N - 60°N and 110°W - 50°W separately for the seasons of December-January-February (DJF), March-April-May (MAM), June-July-August (JJA), and September-October-November (SON). There were 6498, 6624, 6624, and 6552 days in each season, respectively.

2.2. Downscaled Climate Model Projections

Future, daily climate model projections were obtained from the Multivariate Adaptive Constructed Analogs (MACA) statistically downscaled product (Abatzoglou and Brown, 2012). MACA downscales global climate model (GCM) output from the CMIP5 ensemble to higher spatial resolutions while maintaining covariance patterns in multiple variables across space. These downscaled data are designed to ensure physical plausibility across a set of meteorological fields. The downscaling method includes bias correction via quantile mapping followed by a constructed analogs approach, in which a daily GCM synoptic field, or target pattern, is built by identifying

and taking a linear combination of the 30 best predictor patterns from the observational record that are most similar to the GCM synoptic field. An epoch adjustment is employed that removes differences in the means between future and historical time periods to manage instances with no historical analogs under future climate scenarios. The MACA method is performed jointly for temperature and dew point temperature to maintain coherence across those fields.

MACA data are gathered for the period between 2006-2099 at 15 locations across the state of Massachusetts (see Figure 1). These locations were selected to be near major metropolitan areas and to provide good coverage across the state. Five variables were gathered from the MACA dataset, including daily precipitation, minimum and maximum temperature, and minimum and maximum relative humidity. Daily average temperatures and relative humidity were calculated based on the minimum and maximum values and were then used to calculate average daily dew point temperature (see Eq. 8 in Lawrence, 2005). Data were collected for the RCP 8.5 emission scenario from 11 different climate models (see Table 1). These 11 models were chosen from the full set of 20 models in the MACA dataset to 1) ensure they contained relative humidity data needed for the dew point temperature calculation, and 2) avoid the inclusion of two related models from the same institution that may exhibit significant redundancy in model output (Knutti et al., 2013; Steinschneider et al., 2015).

Table 1. Climate models used in this study. All projections were gathered for the RCM 8.5 scenario.

GCMs		
(1) BCC-CSM1-1	(5) CSIRO-Mk3-6-0	(9) IPSL-CM5A-MR
(2) BNU-ESM	(6) GFDL-ESM2M	(10) MIROC-ESM
(3) CAN-ESM2	(7) HADGEM2-ES365	(11) MRI-CGCM3
(4) CNRM-CM5	(8) INMCM4	

We selected the MACA product over other publicly available downscaled products for several reasons. First, the MACA product provides projections of relative humidity needed to calculate dew point temperature, which is important for a thorough assessment of extreme precipitation scaling. Second, the MACA product downscales a relatively large set of GCMs from the CMIP5 database, providing a better quantification of uncertainty compared to dynamically downscaled products based on a smaller set of GCMs (e.g., CORDEX, Jones et al., 2011). Finally, the MACA product is based on the daily, ~4-km resolution gridMET observational product (Abatzoglou, 2013), while a similar downscaled product - Locally Constructed Analogs (LOCA; Pierce et al., 2014) – is based on a coarser gridded observational product (Livneh et al., 2015). Recent comparisons between MACA and LOCA have shown that projected changes in extreme precipitation are much less intense in the LOCA product compared to MACA (Cantu et al., 2020), and in the Northeast US, this was attributed in large part to the differences in extreme precipitation present in the observational training data (Wang et al., 2020). The coarser observational product used in LOCA may have dampened extremes, and so we selected MACA to reduce the effect of this dampening on our inferred scaling rates.

3. Methods

Below we detail three separate analyses that focus on how extreme precipitation scales with dew point temperature, both in observations and in climate model projections, across annual, seasonal, and daily time scales. Multiple statistical methods are used across the different analyses to ensure

robustness of the scaling rates we derive from the data. For the daily time scale analysis, we focus on how extreme precipitation scaling varies with weather regimes prevalent across the Northeast US.

3.1. Annual Maximum

We first assess scaling between precipitation extremes and dew point temperature on an annual time step and at a regional scale. For each ISD-GSOD station (i) and each year (t), we calculate the wet-day mean dew point temperature for that year ($T_{dew,i,t}$) and the annual maximum precipitation ($P_{max,i,t}$). We use mean dew point temperature, but similar results would result using the median given the symmetry of the temperature distribution. Hereafter all references to average dew point temperature refer to wet-day averages (when precipitation is non-zero), which is a preferable metric because it reflects temperature during days without moisture limitation; however, we also conducted all analyses with all-day average dew point temperatures and results do not change substantively.

Because the number of years of data at many of the stations is relatively small, we pool the mean annual dew point temperature and maximum annual precipitation values across stations into a single dataset. Then, following a similar approach to Zhang et al. (2017), we use this pooled dataset and fit a generalized extreme value (GEV) distribution with the location ($\mu_{i,t}$) and scale ($\sigma_{i,t}$) parameters changing linearly with the dew point temperature at station i and year t :

$$P_{max,i,t} \sim GEV(\mu_{i,t}, \sigma_{i,t}, \xi) \quad (1)$$

$$\mu_{i,t} = \beta_{\mu,0} + \beta_{\mu,1}T_{dew,i,t} \quad (2)$$

$$\sigma_{i,t} = \beta_{\sigma,0} + \beta_{\sigma,1}T_{dew,i,t} \quad (3)$$

This model is fit with the `ismev` package in the R statistical software environment (Coles et al., 2001). Note that the regression parameters $\{\beta_{\mu,0}, \beta_{\mu,1}, \beta_{\sigma,0}, \beta_{\sigma,1}\}$ and shape parameter (ξ) are the same for each site, reflecting the pooled estimation approach. We also considered three competing models where: 1) the location and scale parameters are static (i.e., a benchmark model where none of the GEV parameters vary with covariates); 2) only the location parameter varies with dew point temperature (i.e., the scale parameter is assumed the same across all sites, similar to the shape parameter); and 3) the location and log-scale parameters vary linearly with dew point temperature (i.e., we allow for a log-transform in the scale parameter, which is a common approach taken in the literature). Likelihood ratio tests (not shown) indicate that the model formulation in Eqs. 1-3 outperforms these other formulations. In addition, we note that the estimated scale parameters are well above zero and so did not require the log transformation to ensure positive values.

The above model allows dew point temperature to act as both a temporal and spatial covariate. That is, annual dew point variations across space and time are used to explain year-to-year shifts in the distribution of extreme precipitation across different locations. While long-term average dew point differences across locations can help explain some spatial variability in extreme precipitation distributions, it will not be able to explain spatial variations as well as site-specific models. However, the estimation of site-specific models would be severely limited by the paucity of data at many of the sites, leading to significant uncertainty. This motivates our use of a regional model here; this limitation is more carefully addressed using a hierarchical Bayesian model described in Section 3.2 below.

A similar approach to that described in Eqs. 1-3 is also taken using pooled data across the 15 downscaled climate model locations, separately for each of the 11 models. For both the observations and each of the 11 climate models, we then calculate the regional scaling rate between average annual dew point temperature and annual maximum precipitation. The scaling rate is calculated by first estimating the 100-year return period event ($P_{100-yr,i,t}$) for each year and site based on the fitted GEV model above. Then, a linear model is estimated between the log of the 100-year event and the average annual dew point temperature:

$$\log(P_{100-yr,i,t}) = \alpha_0 + \alpha_1 T_{dew,i,t} \quad (4)$$

The scaling rate per degree dew point warming (i.e., $\Delta T_{dew} = 1^\circ\text{C}$) is then calculated as follows:

$$scaling(\%) = 100\% \left[\exp \left(\log \left(\frac{P_{100-yr}|(T_{dew} + \Delta T_{dew})}{P_{100-yr}|T_{dew}} \right) \right) - 1 \right] = 100\% [\exp(\alpha_1) - 1] \quad (5)$$

Finally, we use linear regression to assess regional trends at the annual scale in both annual maximum precipitation and annual average dew point temperature for the observations and the 11 different climate models.

3.2. Seasonal Partial Duration Series

The analysis of annual maxima is useful for exploring extreme precipitation scaling relevant to engineering design statistics, and also for providing a uniform assessment of extreme precipitation trends across time. However, an annual maxima approach ignores useful information if multiple extremes occur in a single year. In addition, extreme precipitation scaling may depend on the storm type (large-scale vs. convective precipitation), which can vary significantly by season (Molnar et al., 2015; Park and Kim, 2017; Schroeer and Kirchengast, 2018). For these reasons, we utilize partial duration series (PDS) calculated by season to further explore extreme precipitation scaling in both the observations and the climate models.

We follow DeGaetano and Castellano (2017) and use PDS of the n largest daily precipitation events for each station, where n equals the number of days with observations divided by 365.25. This value approximates the number of years of observations, and so the PDS will have a similar number of observations to the annual maxima approach. However, the extremes in the PDS may be larger because they are not constrained to one extreme event per year. To ensure independence between events in the PDS, we require a seven-day separation between events.

PDS were calculated separately by season (DJF, MAM, JJA, SON) for each station in the observations and site in the downscaled climate model data. In addition, we also calculate the average (wet-day) dew point temperature by station (or site for the modeled data) and season. We then explore the relationship between the PDS of extreme precipitation and seasonal average dew point temperature across the observations and climate models and how these variables vary across space. We also fit GEV models to the PDS with static parameters (not a function of dew point temperature) by station (or site) and season, in order to assess how these model parameters vary with average dew point temperature by season.

After an exploratory analysis of the data, we develop a hierarchical Bayesian model to estimate a seasonal, regional scaling rate for extreme precipitation with dew point temperature. Similar to the model for annual maxima, each value in the PDS for site i is modeled using a GEV distribution with location and scale parameters that vary linearly with seasonally averaged dew point temperature:

$$PDS_{i,t[j]} \sim GEV(\mu_{i,t}, \sigma_{i,t}, \xi_i) \quad (6)$$

$$\mu_{i,t} = \beta_{\mu,0,i} + \beta_{\mu,1}T_{dew,i,t} \quad (7)$$

$$\sigma_{i,t} = \beta_{\sigma,0,i} + \beta_{\sigma,1}T_{dew,i,t} \quad (8)$$

Here, $t[j]$ indexes the j^{th} value in the PDS in year t , and $T_{dew,i,t}$ is the average dew point temperature for a particular season in year t . The model above differs from the model in Eqs. 1-3 in two important ways. First, the intercept terms $\{\beta_{\mu,0,i}, \beta_{\sigma,0,i}\}$ are allowed to vary by site to enable more flexibility in modeling differences in the extreme precipitation distribution across space. The slope parameters $\{\beta_{\mu,1}, \beta_{\sigma,1}\}$ are still kept the same across sites, thereby acting as a regional scaling factor with dew point temperature. Second, the shape parameter ξ_i is allowed to vary by site in recognition that the fat-tailed nature of extreme precipitation may vary across the domain. However, we employ partial pooling via a regional, truncated normal prior distribution for the shape parameter to help stabilize estimation and share information across sites:

$$\xi_i \sim N(\mu_\xi, \sigma_\xi)T(0, \infty) \quad (9)$$

Here, $T(0, \infty)$ indicates that the prior distribution for ξ_i is truncated to be positive, a choice motivated by uniformly positive shape parameters across the static, at-site models (see above). Similarly, the values for $\sigma_{i,t}$ are constrained to be positive and the values for $\mu_{i,t}$ are constrained to be less than $\min(PDS_i) + \frac{\sigma_{i,t}}{\xi_i}$. The latter constraint is needed to respect the support of the GEV distribution.

All parameters and hyper-parameters of the model $\{\beta_{\mu,0,i}, \beta_{\sigma,0,i}, \beta_{\mu,1}, \beta_{\sigma,1}, \mu_\xi\}$ are given uninformative uniform priors, except for σ_ξ , which is given a relatively uninformative gamma prior with shape equal to 1 and rate equal to 10. The Bayesian model is developed in the STAN probabilistic coding language. Posterior distributions are evaluated using the Hamiltonian Monte Carlo sampling method (Duane et al., 1987). Three chains are run for all parameters with overdispersed initial values using 2,500 burn-in simulations and 2,500 iterations afterwards. Convergence is assessed based on chain mixing using the Gelman and Rubin convergence criterion (Gelman and Rubin, 1992).

The model above is fit separately to the observations and the climate model data by season. Scaling rates are then calculated for each site and season following Eq. 5. However, the scaling rate is calculated for a range of design events (5-year, 10-year, 25-year, 50-year, 100-year) to determine if scaling varies with the magnitude of the event.

3.3. Daily Scaling by Weather Regime via Hierarchical Bayesian Quantile Regression

The analysis in Section 3.2 focused on extreme events by season and identified through a PDS approach. While the separation by season likely helps to isolate major differences in storm type in

the scaling analysis (e.g., convective events in the warm season, stratiform events in the cold season), there may still be a mix of storm types within a given season. Therefore, the analysis in this section further separates data within each season into separate weather regimes (WRs), and then explores extreme precipitation scaling by WR. Because the separation of data into WR further disaggregates a limited dataset, we explore extreme precipitation scaling based on a Bayesian quantile regression technique applied directly to daily data, thereby retaining a sufficient sample size to estimate scaling rates and partially pooling across WRs to stabilize the estimation.

We followed a two-step strategy to identify WRs embedded in the seasonal large-scale atmospheric circulation over the Eastern United States. First, GPH anomalies in each season are projected onto their first J empirical orthogonal functions (EOFs). Here, J is determined to ensure that the selected EOFs explain the majority (90%) of the variance in the data. Next, Hidden Markov Models (HMMs) are fit using the first J principal components (PCs) of the GPH anomalies in each season to partition each day in the record into one of K separate WRs (or states) in that season. We select K such that the difference between the Bayesian information criterion (BIC) for consecutive HMMs fit using $K=2$ to $K=9$ states begins to approach a constant, i.e., the rate of model improvement with additional states begins to slow. This two-step strategy leads to the identification of four WRs within each season (DJF, MAM, JJA, and SON).

We then develop a hierarchical Bayesian quantile regression approach to quantify the scaling rates of extreme precipitation with temperature for a specific precipitation quantile and conditioned on the WRs for each season over the Northeast. The proposed hierarchical Bayesian quantile regression is formulated for site i and day t as follows:

Layer 1: Precipitation-Temperature Scaling

$$\begin{aligned} \ln(P_{i,t}) &\sim \text{Normal}(\mu_{p_{i,t}}', \sigma^2_{p_{i,t}}') \\ \mu_{p_{i,t}}' &= \frac{1-2q}{q(1-q)} w_{i,t} + \mu_{p_{i,t}} \\ \mu_{p_{i,t}} &= \alpha_{i,k(t)} + \beta_{i,k(t)} T_{dew_{i,t}} \\ \sigma^2_{p_{i,t}}' &= \frac{2w_{i,t}}{v_i q(1-q)} \\ v_i &\sim \text{Uniform}(0,100); w_{i,t} \sim \text{Exponential}(v_i) \end{aligned}$$

Layer 2: Scaling Rate by Weather Regime

$$\begin{aligned} \alpha_{i,k(t)} &\sim \text{Normal}(0, 100) \\ \beta_{i,k(t)} &\sim \text{Normal}(\mu_k, \sigma_k^2) \\ \mu_k &\sim \text{Normal}(0,1); \sigma_k \sim \text{InverseGamma}(1,10) \end{aligned}$$

Two layers are embedded within the structure of this hierarchical model. In the first layer, log-precipitation is regressed on dew point temperature, with regression coefficient $\beta_{i,k(t)}$. However, the mean response, as well as the variance, are also dependent on a uniform deviate v_i , a weighting factor $w_{i,t}$, and the quantile of interest, q . This formulation results in an asymmetric Laplace distribution for log-precipitation that emphasizes predictions for a specific quantile of the daily precipitation distribution (Koenker & Machado, 1999; Yu and Moyeed, 2001; Yu and Zhang, 2005).

In the second layer, the regression coefficient $\beta_{i,k(t)}$ is conditioned on the WR present during day t . That is, the regression coefficient at site i that links dew point temperature to the quantile of precipitation will vary by WR, and regression coefficients across all sites will be partially pooled through the use of a parent prior distribution for $\beta_{i,k(t)}$ with time-invariant mean and variance that are WR-specific.

Inferred values of $\beta_{i,k(t)}$ can be translated into scaling rates for extreme precipitation using Eq. 5. Model parameters are estimated using JAGS (Plummer et al., 2003) in the R programming language. JAGS employs the Gibbs sampler and Markov Chain Monte Carlo (MCMC) method for simulating the posterior probability distribution of parameters. We fit the hierarchical Bayesian quantile regression model separately for each season (DJF, MAM, JJA, SON) and for three quantiles of interest ($q = 0.5$ (median), 0.9, and 0.99). The models are fit with 2000 iterations for burn-in and 2000 iterations for posterior simulation across four chains.

4. Results

4.1. Annual Maxima

Figure 2 shows the relationship between precipitation annual maxima and annually averaged (wet-day) dew point temperature across all sites and years. Results are shown separately for each climate model and the observations. Also shown are the 100-year storm estimates as a function of dew point temperature and the estimated scaling rate of the 100-year storm with dew point temperature (expressed as % change per °C).

At the annual scale, extreme precipitation increases with average annual dew point temperature in the observations. The regional scaling rate is estimated to be approximately 5.3% per °C, which is modestly below the theoretical C-C scaling rate of 7% per °C. Across the different climate models, extreme precipitation scaling with annual dew point varies considerably. In some models (CAN-ESM2, MIROC-ESM) the scaling rate approaches the theoretical rate of 7% per °C, while in other models (BCC-CSM1, BNU-ESM, GFDL) the scaling is negative. Across the 11 climate models, the mean regional scaling rate is 1.8% per °C.

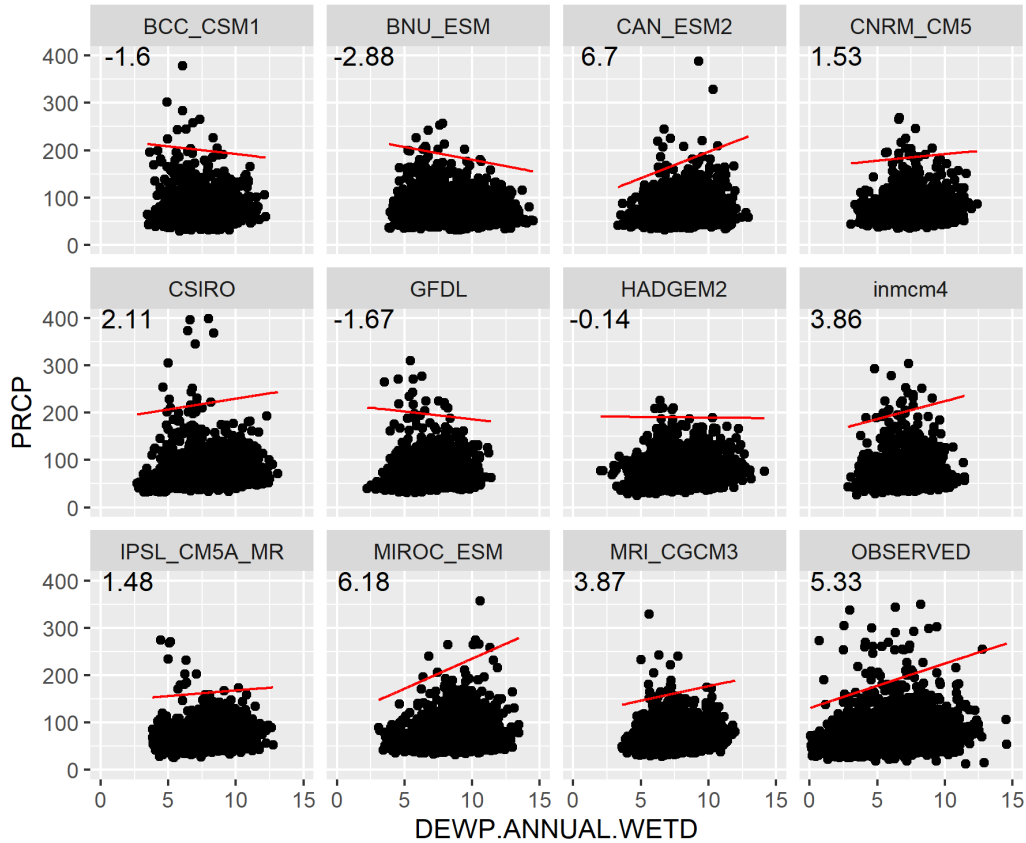


Figure 2. Annual maximum precipitation against annual average dew point temperatures for 11 GCMs and the observations, along with dynamic 100-year storm estimates over the calendar year. The estimated scaling rate of the 100-year storm with dew point temperature (% change per °C) is shown as text.

The variability in scaling rates across the 11 climate models can partially be explained by their differences in dew point temperature and extreme precipitation trends. In all climate models, annual averaged dew point temperature is projected to increase significantly (Figure 3), with linear trends ranging from $+0.39^{\circ}\text{C}$ to $+0.67^{\circ}\text{C}$ per decade. Similarly, in the historical observations, average annual dew point temperatures have increased modestly by approximately $+0.14^{\circ}\text{C}$ per decade between 1948 and 2020. All temperature trends are significant at the 0.001 level. Trends in (log-transformed) annual maximum precipitation are somewhat less consistent across the models and observations. In the observations, annual maximum precipitation has increased significantly across the Northeast region ($p < 0.05$) at a rate of approximately $+0.9\%$ per decade. Over ~ 7 decades (1948-2020), this translates to an approximate 6.7% increase in annual maximum precipitation over the period of record. This increase is only slightly larger than the estimated scaling of the 100-year storm over this same timeframe (a 5% increase), which can be derived based on the estimated scaling rate (5.33% per $^{\circ}\text{C}$, see Figure 2) and the observed degree of warming over the period of record (0.95°C).

In the climate models, trends in annual maximum precipitation range from -0.5% to $+3.0\%$ per decade, with an average change of 1.4% per decade (similar to the observations). We note that the negative trends in annual maxima are not statistically significant (BCC-CSM1, BNU-ESM), while all positive trends are statistically significant at the 0.01 level for the remaining climate models,

with the exception of GFDL (which exhibits a near-zero trend in annual maxima). The precipitation annual maxima generally trend upward in those models that exhibit positive scaling rates and trend downward or are flat in those models that exhibit negative or near-zero scaling rates (see Figure 2). This suggests that the scaling rates in Figure 2 are influenced by whether extreme precipitation trends coincide with dew point temperature trends. That is, for most models with significant positive trends in both temperature and precipitation, scaling rates are higher, and for most models with positive trends in temperature but near-zero or negative trends in precipitation, scaling rates are lower. There are some exceptions to this pattern (e.g., the HADGEM2 model exhibits a positive trend in annual maximum precipitation but has a near-zero scaling rate), but it generally holds across most models.

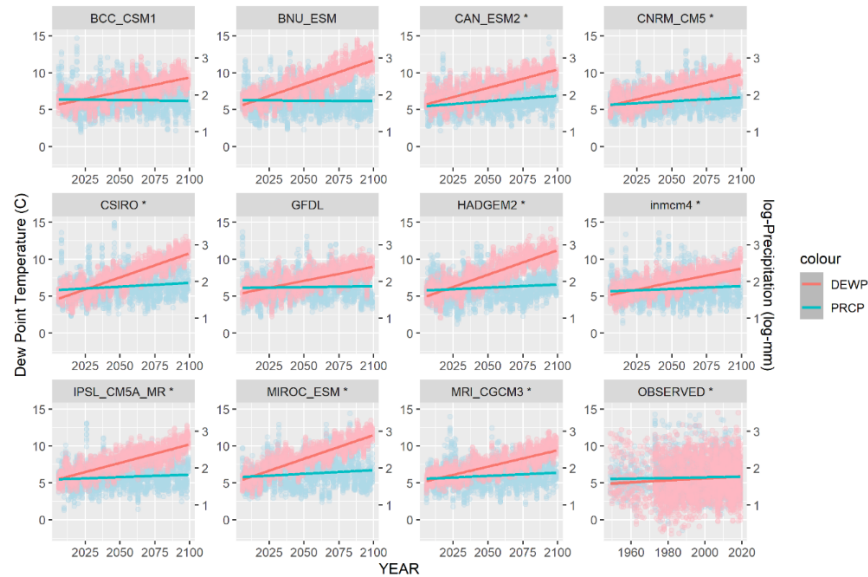


Figure 3. Linear time trend in annual mean dew point temperature and annual maximum precipitation pooled across locations, shown separately for 11 GCMs and the observations. Statistical significance ($p < 0.05$) in the trends for log-precipitation is indicated by *. All temperature trends are statistically significant at the 0.001 level.

4.2. Seasonal Partial Duration Series

PDS are calculated for all sites in both the observational and downscaled climate model output, separately by season. Figure 4 shows how extremes within these PDS vary with average seasonal (wet-day) dew point temperature, after pooling all data together across sites. In the observations, precipitation extremes exhibit a clear increase with dew point temperature, and much of this variation occurs across the seasons. In winter, when dew point temperatures are lowest, precipitation extremes also tend to be relatively small (daily maximum value of 128 mm across all sites). In the spring, fall, and especially summer, dew point temperatures increase significantly, and the largest precipitation values across stations grow to over 300 mm. A similar pattern for winter, spring, and fall is observed in the climate models. However, across almost all of the models (with the exception of inmcm4), summer extreme precipitation events deviate from the pattern in the observations and are relatively muted compared to those in the spring and fall seasons. This downward shift in summer extremes compared to the other seasons is especially pronounced in the CNRM-CM5, GFDL, MIROC-ESM, and MRI-CGCM3 models. While a diagnosis of these differences in seasonal extremes is beyond the scope of this work, it may be related to the difficulty

of climate models to simulate localized convective events or challenges that such localized events present to climate-analog approaches for statistical downscaling. Regardless, the deviation of summer extremes in the downscaled climate model output from that of the observations suggests that caution is needed when using the downscaled climate model data.

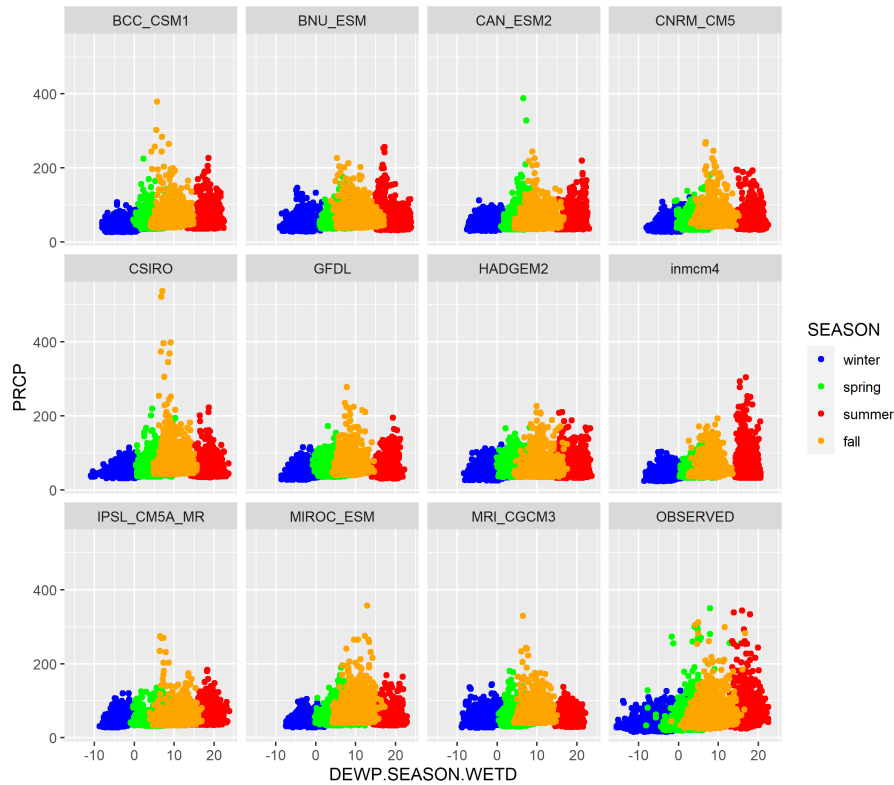


Figure 4. Partial duration series of precipitation events against seasonal averaged dew point temperature, shown separately by season and for 11 GCMs and the observations.

Figure 4 shows that variations in dew point temperature across seasons is correlated with the magnitude of precipitation extremes across those seasons. It is unclear, *a priori*, whether this relationship suggests that dew point temperature increases cause larger precipitation extremes, or just that the mechanisms of precipitation that lead to larger precipitation extremes happen to occur in seasons with larger dew point temperatures. To explore this issue further, Figure 5 shows the seasonally averaged dew point temperature and PDS values across the 93 observational stations in the Northeast region, while Figure 6 shows the relationship between these two variables. Figure 5 shows that from winter to summer, average dew point temperatures increase across the region, and within each season, there is a clear dew point temperature gradient from southern and coastal locations towards inland and northern locations. Those same gradients are present in the average extreme precipitation data. This is seen more clearly in Figure 6. In all seasons, but especially in summer and fall, there are clear positive relationships between seasonal average dew point temperature and extreme precipitation across sites. These relationships are all significant at the 0.01 level and suggest that the relationship between dew point temperature and extreme precipitation in Figure 4 are not driven (exclusively) by seasonally varying storm types, as within a season these relationships are still present.

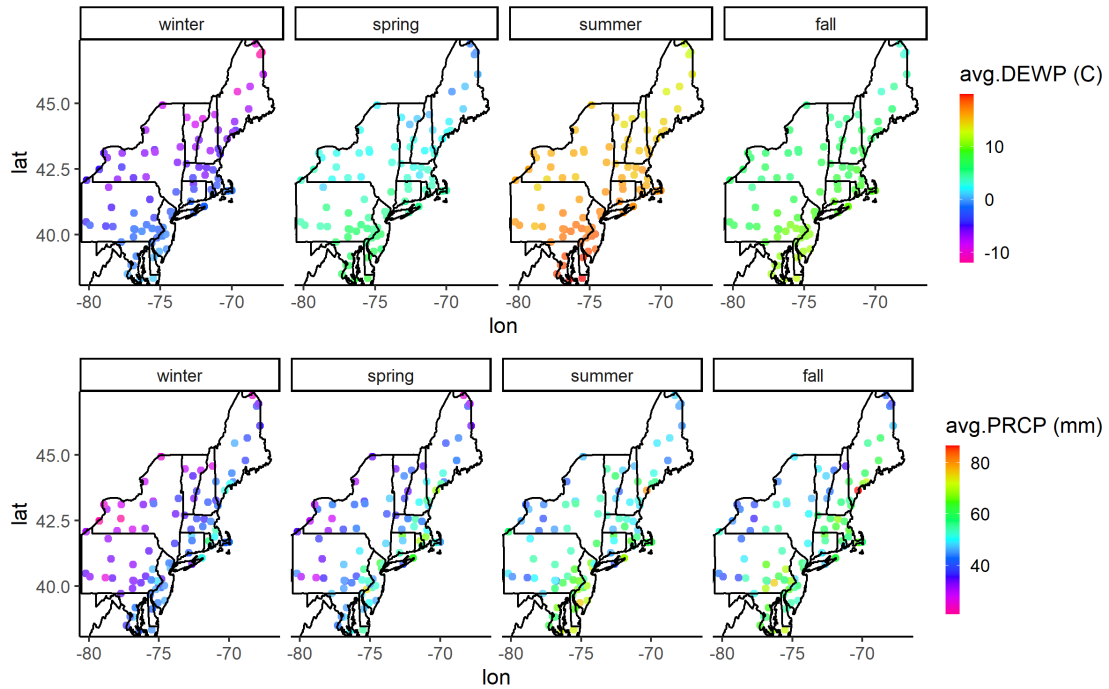


Figure 5. Observed average dew point temperature and average extreme precipitation magnitude by season.

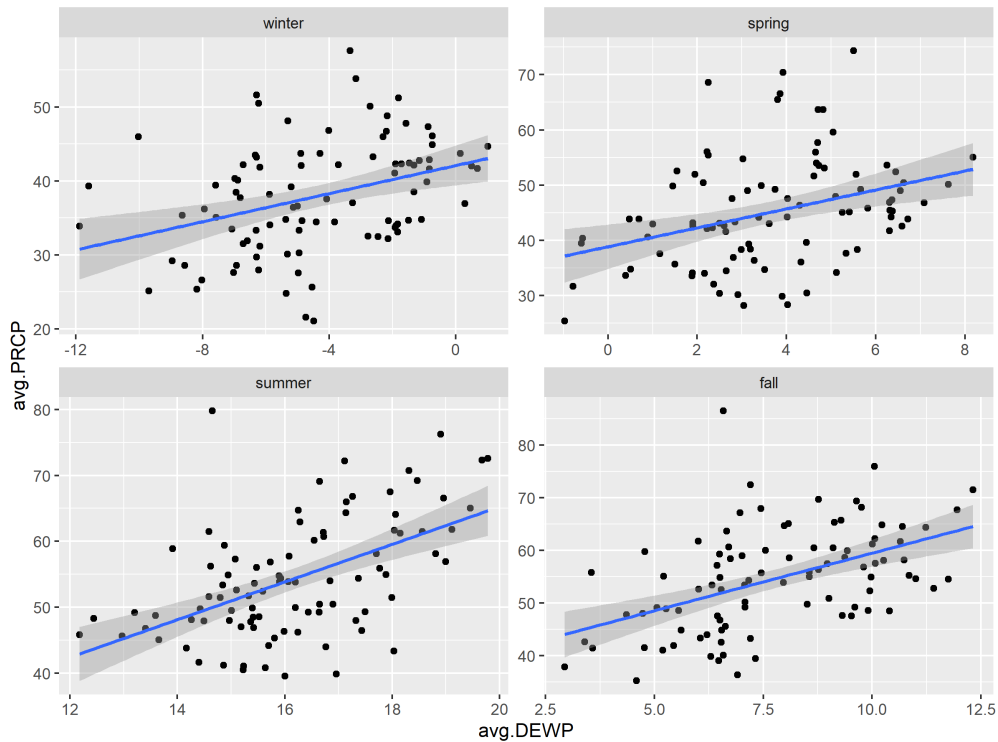


Figure 6. Observed average extreme precipitation vs. average dew point temperature by season. Each point represents the long-term average of both variables for a particular station. All linear relationships are significant at the 0.01 level.

Still, it may be possible that the spatial gradients in extreme precipitation and dew point temperature are not causally related. For instance, near the coastline where atmospheric moisture content (and dew point temperatures) are higher, storm tracks may also be more common, leading to a spurious spatial correlation between the two variables. To explore this, Figure 7 shows spatially averaged log-transformed extreme precipitation versus dew point temperatures by season. That is, in each year, we average the seasonal, log-transformed values of the PDS series across all sites and compare these to the seasonal dew point temperatures averaged across sites. In this way, all spatial variability has been averaged out, leaving only a regionally-averaged signal of extreme precipitation and dew point temperature through time. Results show that regionally-averaged extreme precipitation and dew point temperature are significantly related ($p < 0.05$) in the spring, summer, and fall but not for winter. In addition, the relationship in the spring is driven by a few outliers, which when removed leads to an insignificant relationship. The estimated regressions suggest that in summer and fall (where the relationships are strongest and most robust), extreme precipitation increases by 2.9% and 1.8% per $^{\circ}\text{C}$, respectively. Given the large spatial domain over which the data are averaged, these scaling relationships are notable. Overall, these results coupled with those in Figure 6 suggest a causal relationship between dew point temperature and extreme precipitation, especially in the warm season.

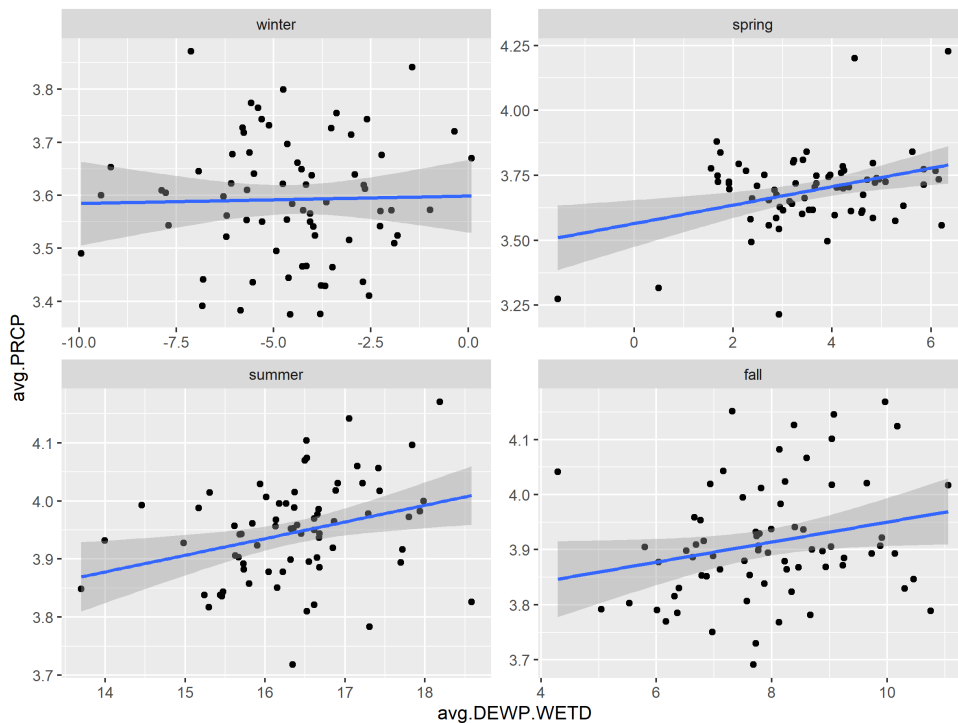


Figure 7. Observed station-averaged, log-transformed extreme precipitation vs. average dew point temperature by season across all sites. Each point represents the annual value of both variables averaged across stations. All linear relationships are significant at the 0.01 level.

To understand better how properties of extreme value distributions for precipitation vary with dew point temperature, Figure 8 shows static GEV parameter estimates at each of the 93 observational stations versus the average dew point temperature, separately by season. Results show that the location parameter of the GEV increases with average dew point temperature, and this relationship becomes stronger in warmer seasons. A similar but stronger relationship is seen for the scale

parameter, especially in the summer and fall seasons. All linear relationships between the location and shape parameters and dew point temperature are significant at the 0.01 level, with the exception of the scale parameter in winter ($p=0.11$). For both location and shape parameters, there is little evidence that these relationships to dew point temperature are non-linear. In particular, Figure 8 supports the use of a linear relationship (rather than exponential relationship) between the scale parameter and dew point temperature, despite the fact that the exponential relationship is more common in non-stationary GEV models. The results also suggest that the shape parameter does not vary significantly with dew point temperature ($p>0.05$ for all seasons). Finally, many of the relationships in Figure 8 are noisy; some of this noise is likely related to limitations of dew point temperature as an explanatory variable for the GEV parameters. However, some of the noise in Figure 8 is likely related to the high degree of sampling uncertainty around GEV parameter estimates, especially for the shape parameter and for those stations with relatively limited data (< 20 years). This suggests that more robust estimates of GEV parameters and their variations with dew point temperature will support a better assessment of how design storms scale with dew point temperature. We employ the Bayesian model described in Eqs. 6-9 for this purpose.

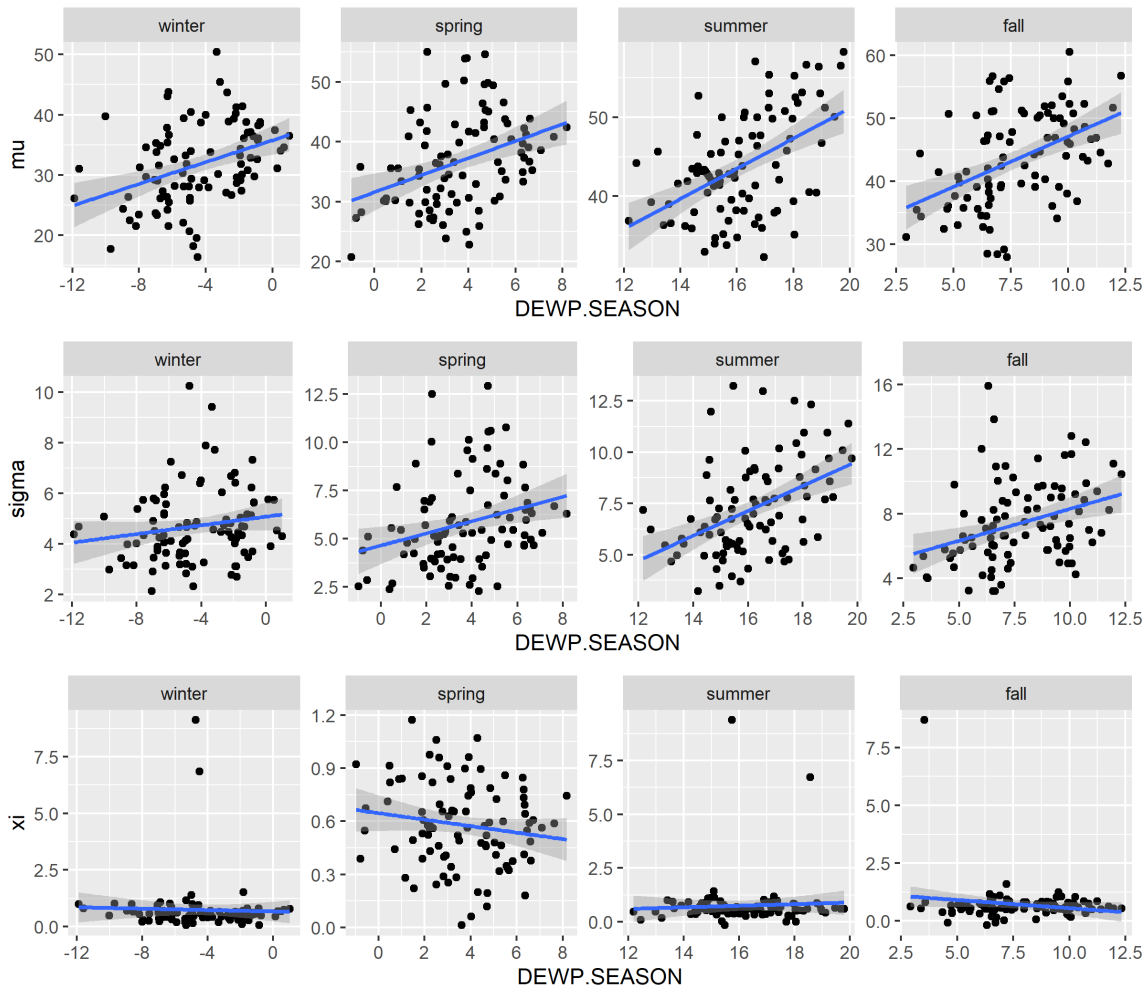


Figure 8. Static GEV parameters against average seasonal dew point temperature across observational stations, with linear model fit also shown.

Figure 9a shows the posterior mean estimates of scaling rates (Eq. 5) for the 100-year storm with dew point temperature across all sites. The distributions of scaling rates across sites are shown separately by climate model and for the observations. Figure 9b shows the median scaling rate across sites for each of the 11 climate models and for the observations. Several insights emerge from Figure 9. First, in the observations there are significant variations in the distribution of scaling rates across seasons. Scaling is largest in the summer, when scaling rates across sites range from +4% to +22% per °C. The median scaling rate across sites is +11.4% per °C. In the fall, scaling rates are somewhat lower, with a median rate around +2.6% per °C and a range across sites between -2.5% and +7% per °C. In spring, scaling rates are near zero across sites. The winter shows slightly lower scaling rates than zero, but when considering the entire posterior distribution (rather than just the posterior mean), zero lies well within the credible intervals for scaling rates across sites.

There is significant variability in the scaling rates estimated for the 11 climate models. In summer, the distribution of scaling rates across sites ranges from below -6% to over 11.5% per °C. Much of this variability is linked to inter-model differences, similar to the annual scaling rates in Figure 2. For instance, the BCC-CSM1, CAN-ESM2, and CNRM-SM5 models exhibit summer scaling rates comparable to those in the observations, while the BNU-ESM, CSIRO, and INMCM4 models all exhibit negative scaling rates. Interestingly, some models that show high summer scaling rates in Figure 9 (BCC-CSM1) showed negative scaling rates when examining annual maxima (see Figure 2). This may be linked to the apparent downward bias in summer extremes in the model (see Figure 4), which would lead to less summer extremes being included in the annual maxima series. We also note that scaling rates in some climate models are significantly higher in the winter and spring than suggested by the observations. In winter, the median scaling rate across sites and models is +2.6% per °C, with some models showing scaling rates as high as +6.4% per °C when aggregated across locations. We note that dew point temperatures in the climate models reach significantly higher levels in the climate models towards the end of the 21st century compared to the range of temperatures seen in the observed record. This may lead to a larger scaling rate if extreme precipitation scaling with dew point temperature is dependent on the absolute magnitude of dew point temperature exceeding some minimum threshold.

To this point, scaling rates have been presented for one return period (the 100-year event) and only using posterior mean parameter estimates. However, the rate of scaling may vary across the magnitude of events, and uncertainty should be propagated to better understand the range of plausible scaling rates supported by the data. In Figure 10, the full posterior distribution of scaling rates is shown for a particular site (Boston MA) and different return periods, separately by season. The theoretical scaling rate of +7% per °C is shown for comparison. Two major insights emerge from Figure 10. First, the posterior median scaling rate increases slightly as return periods increase. That is, 50- and 100-year events grow somewhat faster with warming dew point temperatures compared to 5- and 10-year events. This is consistent with the theory that as the intensity of a storm grows, the increase in precipitation should begin to mirror the increase in available atmospheric moisture (Allan & Soden, 2008). However, we note that the differences in scaling rate across return periods is small. Second, there is significant uncertainty around the scaling rates of extreme precipitation that grows with return period, particularly in the warmer seasons. For example, in the summer the 95% credible interval for the 100-year event scaling rate ranges from +7.46 to +18.6% per °C. This range is as large as the median scaling rate itself (10.6% per °C).

Notably, after accounting for uncertainty, the theoretical scaling rate of +7% per °C is within or nearly within the 95% bounds of the estimated scaling rates for all return levels across summer and fall.

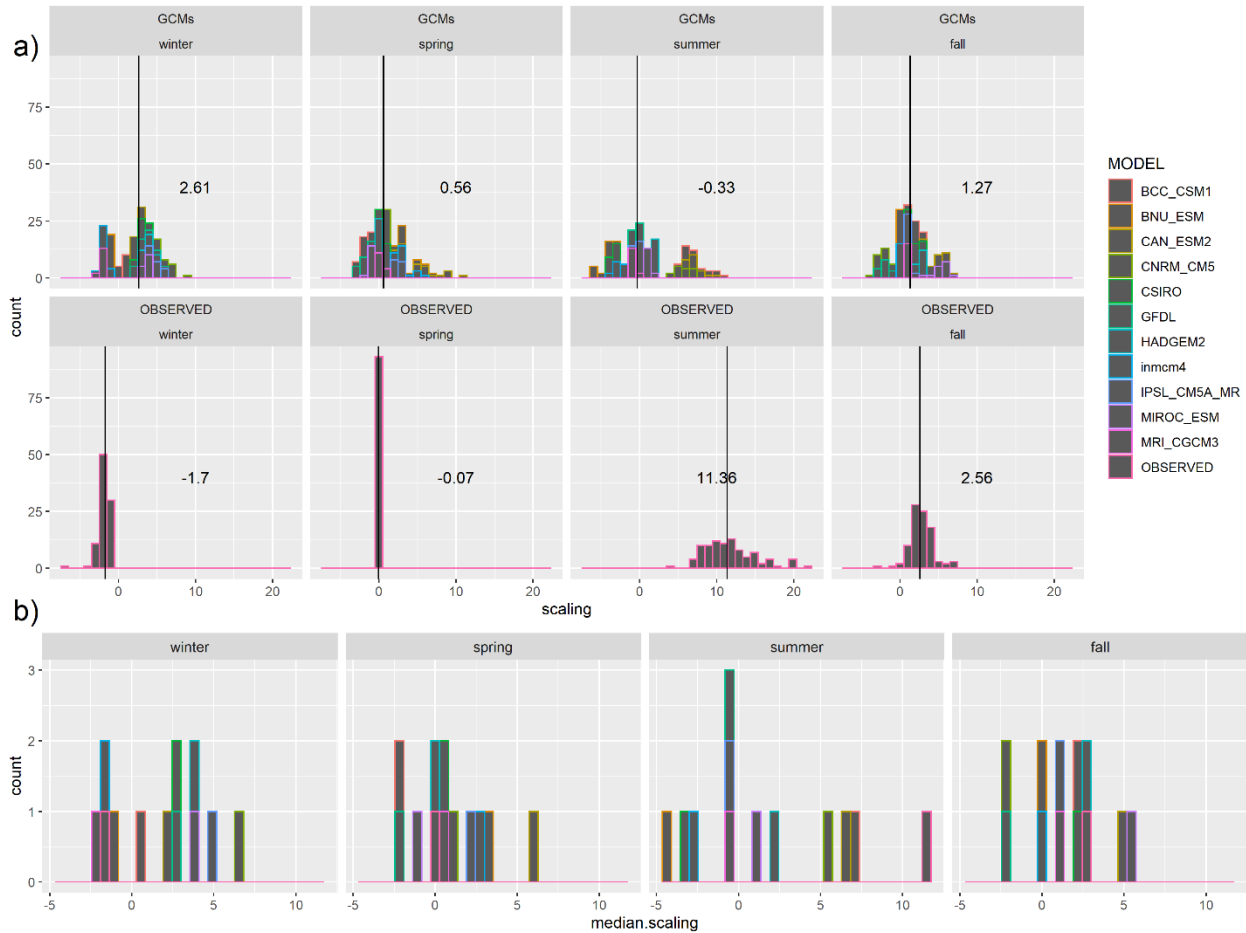


Figure 9. a) Distribution of posterior mean scaling rate with dew point temperature across sites, shown by season. Scaling rates are shown separately for the observations and each GCM. Median scaling rate across sites is shown by vertical line and text. b) Distribution of median scaling rate across sites by model.

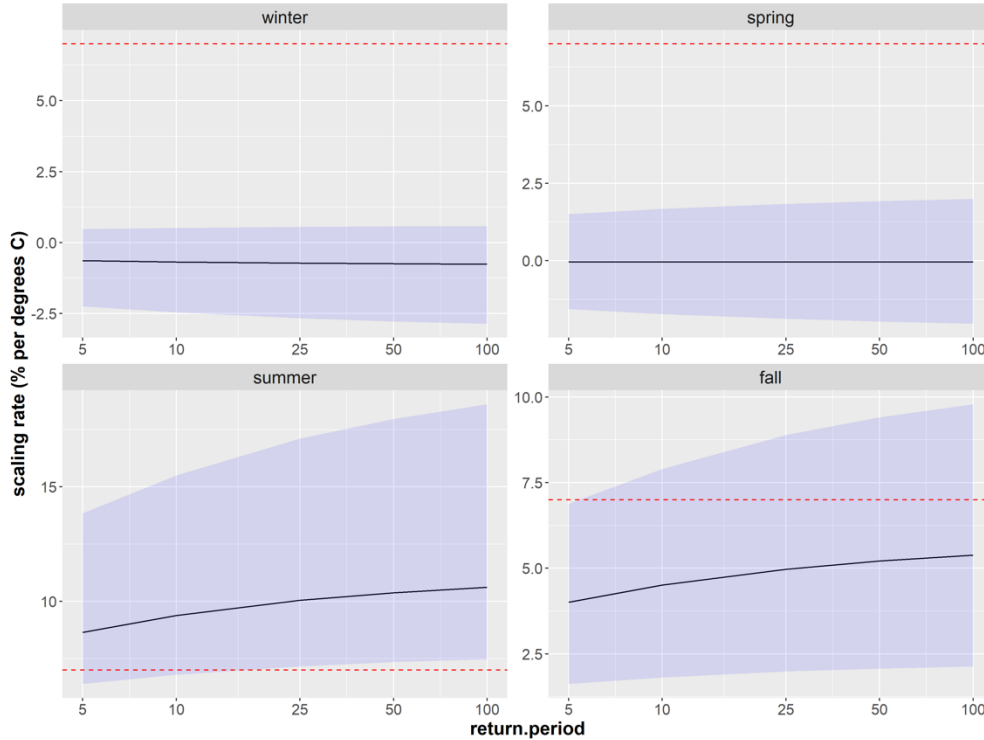


Figure 10. Posterior median and 95% credible interval of the scaling rate for different extreme precipitation return levels with dew point temperature for one site (Boston MA), shown by season. The theoretical C-C scaling rate of +7% per °C is shown in red for comparison.

4.3. Daily Scaling by Weather Regime

Figure 11 shows composites of 500-hPa GPH anomalies for each of the WRs identified by season. In DJF (Figure 11a), WR1 exhibits a ridge centered over the Hudson Bay, which is located between two troughs anchored over the Gulf of Alaska and off the eastern US coastline. This pattern is reversed in WR3. WR2 exhibits a ridge directly over the Northeast US as part of a broader wave train spanning North America. WR4 shows a similar pattern with opposite polarity. The WRs in MAM (Figure 11b) and SON (Figure 11d) are similar to those in DJF, but the GPH anomalies are slightly weaker and some of the patterns (particularly WR4) do not have an analogue in DJF. In JJA (Figure 11c), the WRs are much weaker and more localized around the Northeast US.

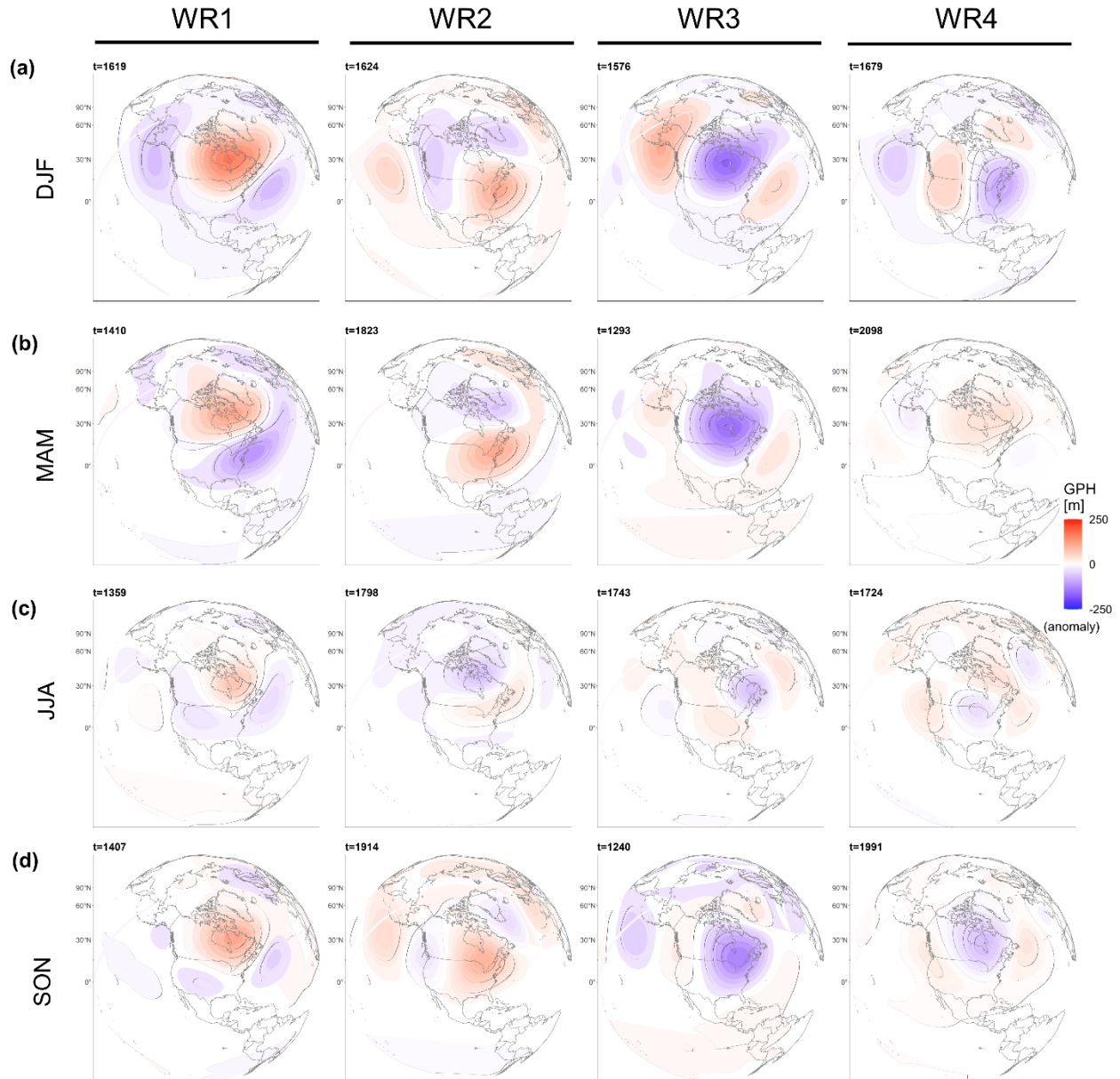


Figure 11. Composites of 500-hPa GPH anomalies [m] for days categorized under each WR in a) DJF, b) MAM, c) JJA, and d) SON. The number of days (t) classified under each WR and season over the entire period (1948-2020) is also shown.

To illustrate the connection between local weather and WRs, Figure 12a,b shows the average precipitation and dry-bulb temperature anomalies by site and WR in DJF. WR1 exhibits relatively wet conditions over the Northeast, particularly along the coast, with near average temperatures across the entire domain. Conversely, WR3 is slightly dry along the coast, but exhibits the same near-average temperature conditions as WR1. WR2 tends to be warmer than average, especially in the south, with slightly above average precipitation in the northwest of the domain. WR4 is dry and cold throughout much of the western and central Northeast US.

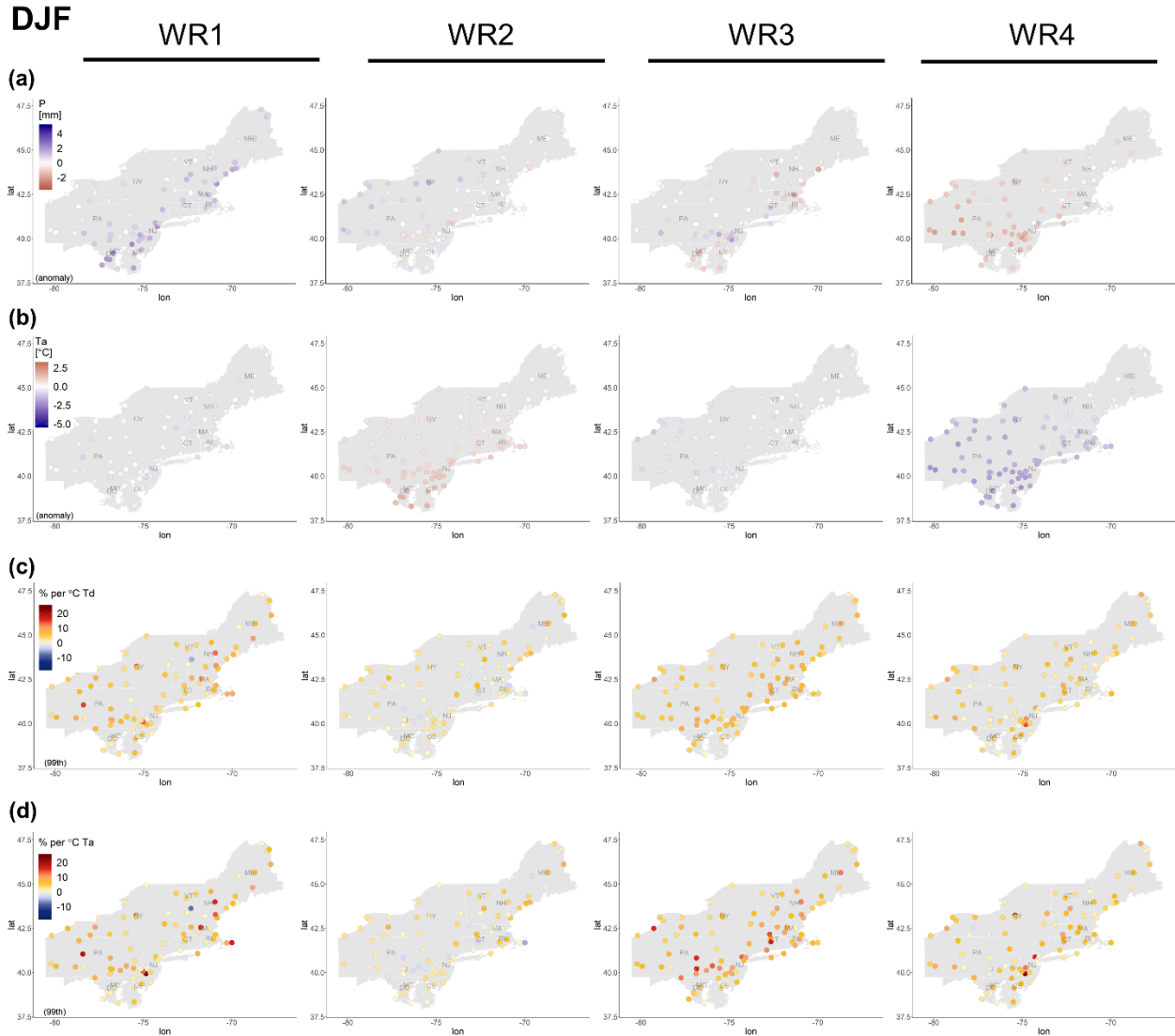


Figure 12. Characteristics of the regional climate including anomalies of (a) precipitation (P) and (b) dry-bulb temperature (T_a), and C-C scaling rates (in % per $^{\circ}\text{C}$) conditioned on four WRs for (c) dew point temperature (T_d) and (d) T_a inputs at the 99th precipitation percentile in the DJF season.

A key question being addressed in this work is how P-T scaling rates vary across the Northeast based on these background atmospheric circulation patterns and climate conditions across seasons. We first examine at-site (posterior mean) estimates of P-T scaling rates for the highest intensity class ($q=0.99$), shown for both T_d and T_a in DJF in Figure 12c,d. In winter, most sites feature positive scaling rates under all WRs, with only a handful of sites exhibiting either near-zero or negative scaling rates. However, in WR2, which exhibits the warmest conditions, scaling rates tend to be lower than the other WRs and more are slightly negative. We did not detect any significant spatial correlation amongst posterior mean scaling rates across sites, based on Moran's I spatial autocorrelation test (Moran, 1950; Gittleman & Kot, 1990). This result is consistent across seasons. Also consistent across seasons, scaling rates using T_d are mostly positive and tend to be moderately larger than rates based on T_a , which can often be negative.

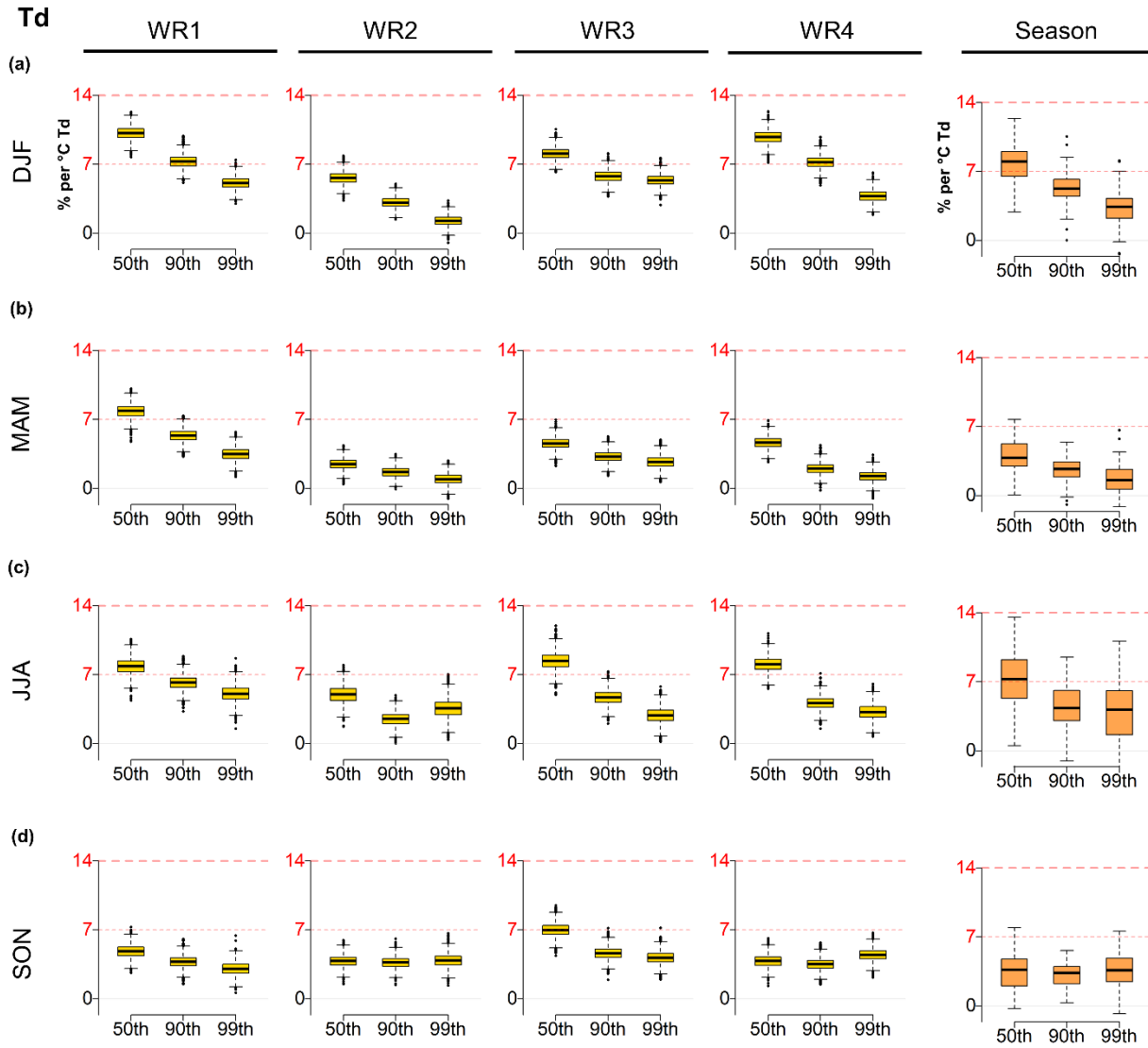


Figure 13. Comparison of the regional C-C scaling rates (μ ; posterior distribution of scaling rates) across the Northeastern United States (in % per $^{\circ}\text{C Td}$) based on the dew point temperature (T_d) for 50, 90, and 99th percentiles in each weather regime (WR) and seasons of a) DJF, b) MAM, c) JJA, and d) SON.

The results above suggest that regional estimates of P-T scaling rates may be better suited to understand major patterns in P-T scaling with WR. These regional estimates are shown in Figure 13, which presents the posterior distribution of the Northeast-wide P-T scaling rate (i.e., μ_k) for each WR, season, and precipitation percentile.

Three main results arise from Figure 13. First, the results suggest that P-T scaling rates do not vary significantly across WRs in most cases. There are a few exceptions, including lower scaling rates estimated for WR2 in DJF and higher scaling rates estimated for WR1 in MAM. However, besides those cases, the posterior distribution of regional P-T scaling across WRs for each unique season

and precipitation percentile exhibit significant overlap. This indicates that differences in scaling rates between WRs are generally inconsequential.

Second, there are significant variations in P-T scaling rates by season. When WRs are excluded from the analysis, winter and summer have the largest scaling rates, which range approximately between 7-8%, 4-5%, and 3-4% per °C Td for $q=0.5, 0.9, \text{ and } 0.99$, respectively. These rates are significantly larger than those for spring (~4%, 3%, 2%) and fall (~4%, 3%, 4%), particularly for the lower quantiles. Note that all regional, posterior median scaling rates are positive when using Td (the minimum rate is 0.9% per °C for WR2 in MAM and $q=0.99$).

Finally, across almost all WRs and seasons, the regional P-T scaling rates decrease when reevaluated on larger precipitation percentiles. This effect is most prominent in the winter, but is also present (albeit weaker) in the spring, summer, and for two WRs in the fall. There are a few exceptions when this pattern is absent, including WR2 in JJA and WR2 and WR4 in SON. However, the general decline of scaling rate with precipitation percentile explains more variability (30%) in the total posterior dataset for μ_k compared to either season (20%) or WR (1%), as estimated using an ANOVA evaluated on all posterior samples across these three factors. An analysis of outliers suggests this effect is due to a small number of storms with heavy precipitation occurring at low temperatures (not shown).

These results exhibit notable differences from the scaling experiments conducted on the seasonal PDS data, e.g., significantly higher scaling rates in non-summer seasons. This suggests that the inferred scaling rate can vary significantly depending on the statistical approach taken, although all methods do suggest positive scaling with higher temperatures. Finally, there is some variability in scaling rate across WRs, but this variability tends to be less than that seen across percentiles.

5. Synthesis of Results and Recommendations

The analysis of the observations suggests that extreme precipitation scales significantly with dew point temperatures across the Northeast region, but this scaling is dependent on season and the type of analysis employed to infer the scaling rate. While the annual scaling rate (5.33% per °C, see Figure 2) estimated for the region approaches the theoretical C-C scaling rate of 7% per °C, the seasonal PDS analysis suggests that much of this annual scaling is driven by scaling in the warm season (summer and fall). While all seasons showed a clear spatial correlation between dew point temperatures and extreme precipitation (Figures 5 and 6), these relationships were strongest in summer and fall, and only those latter seasons exhibited a robust relationship between regional dew point temperatures and extreme precipitation through time (Figure 7). The hierarchical Bayesian model confirmed that extreme precipitation scaling was only present in the observations in the summer and fall when examining PDS data, with the largest signal during peak summer (Figure 9).

However, when examining scaling rates at the daily scale using a quantile regression approach and conditional on weather regime, precipitation scaling with warming was more consistent across seasons (Figure 13). In particular, scaling rates in winter and spring were much higher than those seen for the PDS analysis, never fell below 3% per °C, and on average were around 5% per °C regardless of season. In addition, scaling did not vary that significantly by weather regime.

The downscaled climate model data showed very different scaling rates compared to the observations. On an annual scale, there was significant variability in scaling rates across models (Figure 2), much of which appeared driven by whether models exhibited converging or diverging trends in extreme precipitation and dew point temperatures. However, it is difficult to interpret whether the trends in extreme precipitation relate to how extreme precipitation scales with dew point temperature in the models, or if those trends are dominated by changes in circulation within the models that counteract any effect caused by increasing atmospheric moisture content. Thiabeault and Seth (2015) showed that CMIP5 projected trends in total summer precipitation in the Northeast were significantly influenced by how models represented key features of atmospheric circulation, such as the North Atlantic Subtropical High (NASH). While most models projected the NASH to shift westward in the future, 20th century biases in the longitudinal location of the NASH largely determined whether summer precipitation was projected to increase or decrease in the Northeast. This suggests that model-based scaling rates needs to be interpreted with care.

Arguably, model-based estimates of scaling may be most interpretable when inter-model spread is relatively low and during cold-season months when larger-scale circulation rather than convective processes drive precipitation. Indeed, the downscaled data from many of the climate models show clear downward biases in summer precipitation extremes as compared to the observations (see Figure 4). While it is unclear if these biases are related to challenges in simulating convective events or the specific downscaling methodology used, these biases do raise concerns regarding interpretation of model-based scaling rates in the summer. However, model-based extreme precipitation in the cold season appears to behave similarly to the observations, at least with respect to how they scale across seasons with dew point temperature (Figure 4), and projected scaling rates are more consistent across models in cooler season months compared to the summer (see Figure 9). In these cool season months, particularly winter, the models estimate positive scaling rates (median rate of 2.6% per °C across models), even though the observations show near-zero scaling rates for the winter. Since dew point temperatures are projected to increase well above their historical ranges in the climate model projections, this suggests that scaling rates may be linked to the absolute magnitude of dew point temperature (i.e., a nonlinear relationship between dew point temperature and precipitation), although more work is needed to confirm this hypothesis.

Overall, results suggest that extreme precipitation does indeed scale with dew point temperatures in the Northeast United States. The results of this work suggest the following conclusions about extreme precipitation scaling with warming in the Northeast US and within the state of Massachusetts:

- Observations show that scaling of extreme precipitation with increasing temperature is positive across the Northeast US, with scaling rates that vary between 0% and 11% per °C, depending on the season and type of statistical analysis used.
- While PDS-based observed scaling is mostly limited to the warm season, model-based results and those based on daily observations suggest extreme precipitation scaling with dew point temperature is also plausible in the cold season as temperatures warm.
- Climate model based scaling rates should be used with care due to biases in precipitation extremes, especially in the warm season.

- When averaged across analyses (annual maxima; seasonal PDS-based analysis; daily quantile regression) and seasons, scaling rates across the Northeast US average somewhere between 3% - 5% per °C.

Based on these results, we recommend that design storms across the state of Massachusetts be scaled at the theoretical C-C rate of 7% per °C.

We forward this recommendation for two primary reasons. First, our results show that empirical scaling rates vary around this theoretical scaling rate, deviating above or below it depending on the season and analysis used. Second, when averaged across our different analyses and seasons, empirical scaling rates are slightly below 7% per °C, ranging between 3% - 5% per °C. However, all scaling rates derived in this work are based on daily data, yet the state seeks updates to design storms at both daily and sub-daily levels. At sub-daily timescales, there is significant debate about whether scaling rates are larger than the theoretical C-C rate, with some forwarding physical arguments to support a super C-C scaling rate at sub-daily timescales upwards of 14% per °C (Lenderink et al. 2017). Therefore, the adoption of a 7% per °C scaling would provide a margin of safety for sub-daily events, rather than using a lower scaling between 3% - 5% per °C, and this choice is consistent with the recommendations forwarded in Zhang et al. (2017).

6. Implementation of Recommendations for Massachusetts – Updated IDF Curves

To implement the above recommendations, we have retrieved gridded (30 arc-second resolution) design storm estimates from the NOAA Atlas 14 database (Perica et al., 2019) for a range of durations and return periods (see Table 2). We have updated these intensity-duration-frequency (IDF) curves by scaling all values by 7% per °C for a range of temperature changes (0°C to 8°C warming at 1°C increments), which is the range of warming projected by the CMIP5 ensemble across the state of Massachusetts. Figure 14 shows an example of one design storm (5-year, 24-hour event) under baseline conditions (no warming, 0°C) and scaled based on 3°C warming. Figure 14 suggests that storm rainfall depth related to the 5-year, 24-hour event will increase from 4.16 in to 5.10 in when averaged over the state of Massachusetts for a 3°C warming scenario.

Table 2. List of return periods and durations for design storms updated via C-C scaling across the state of Massachusetts.

Return Period (year)	Duration
1	5 minute
2	10 minute
5	15 minute
10	1 hour
25	2 hour
50	3 hour
100	6 hour
200	12 hour
500	24 hour
1000	48 hour

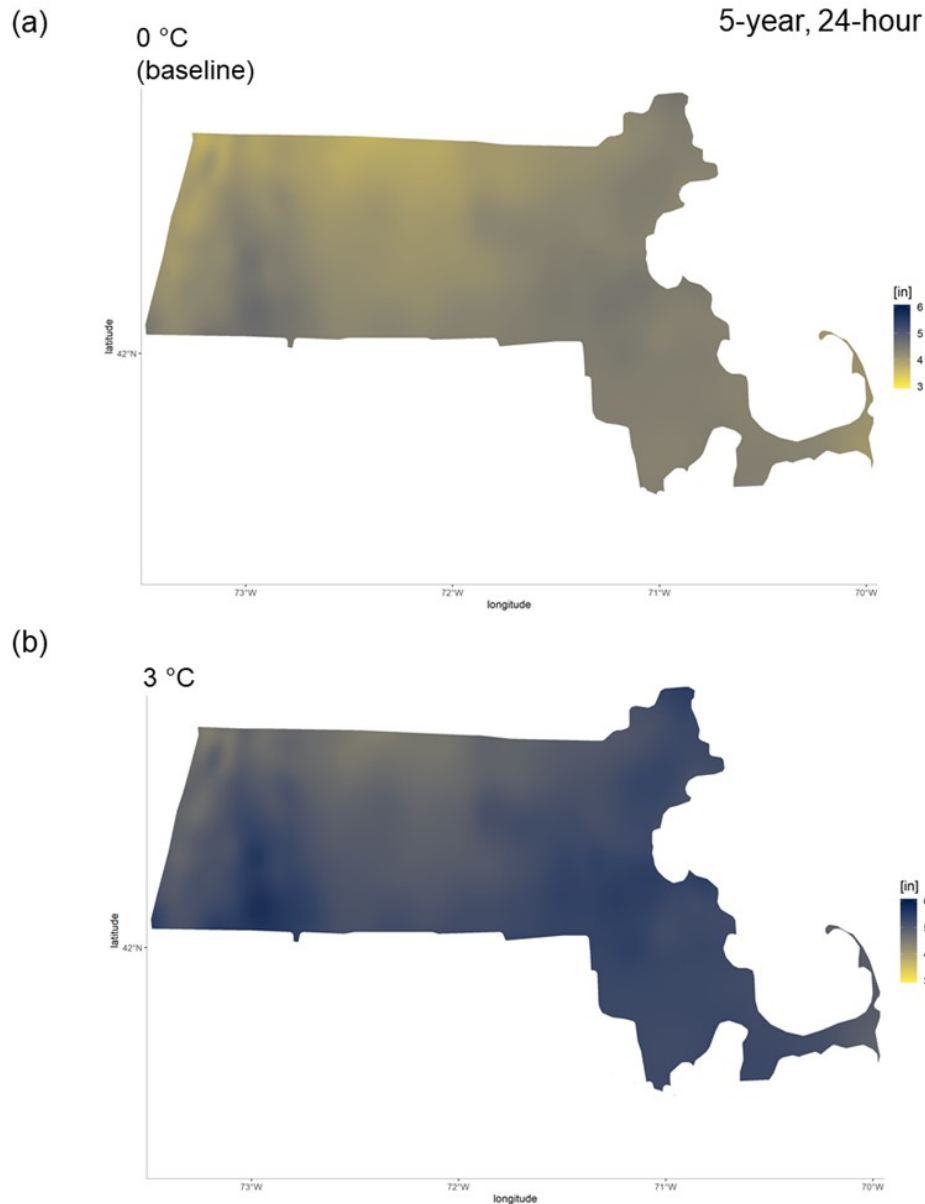


Figure 14. The 5-year, 24-hour precipitation event under baseline conditions (no warming, 0°C) and scaled based on 3°C warming across the state of Massachusetts.

To select an updated IDF curve for use, decision-makers should consult projections of warming for a given location within the state and for a particular target decade, as provided on the ResilientMA website (<https://resilientma.org/>). Once the warming scenario has been selected, gridded, scaled IDF curve values associated with that degree of warming and location can be downloaded and used directly for design purposes. For example, Figure 15 shows projected warming scenarios for the Nashua River Basin based on downscaled CMIP5 projections. If a decision-maker is interested in planning for the target decade of 2050 and under the RCP 8.5 scenario, then they would select the annual temperature change of 5.44°F, or 3°C. The updated IDF curves associated with a 3°C warming scenario can then be selected for use. In Figure 16, we

provide warming scenarios for the 2030s, 2050s, 2070s, and 2090s based on the MACA downscaled data for RCP 4.5 and RCP 8.5 for 20 basins across the state of Massachusetts.

The above approach has the benefit of integrating well with standard practices for design and planning used across the state of Massachusetts. Engineers and planners across the state are familiar with the Atlas 14 product and use it regularly to inform infrastructure design and hazard assessments. By providing updated Atlas 14 values via thermodynamic scaling, the product of this work leverages the significant resources and vetted analyses that went into the original development of Atlas 14, and produces a product that will be readily understood by practitioners across the state. The key advance provided here is an updated set of IDF curves that account for thermodynamic climate change, is based in theory, and is supported by empirical evidence. This will allow engineers and planners to integrate the effects of climate change directly into their current protocols for design and planning.

Location Info ✕

Average Temperatures (Projected)

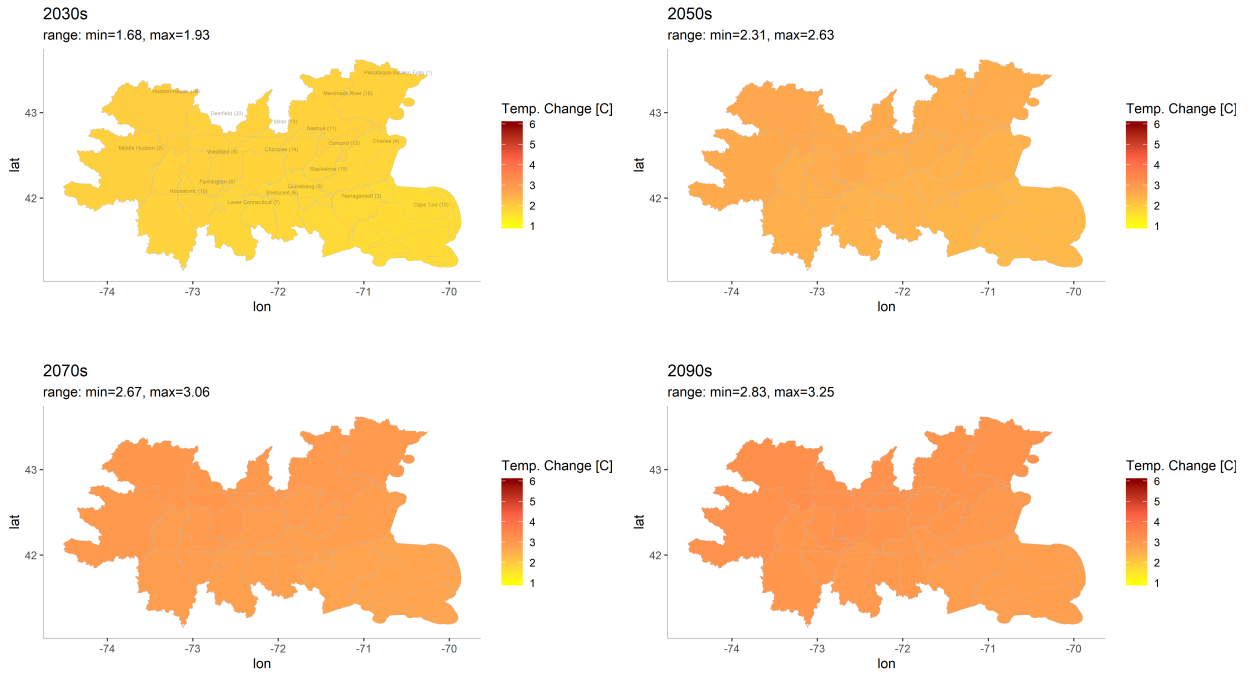
Table shows estimated 50th percentile values for projected change in Average Temperature. The value highlighted in dark green is the value corresponding to the season, decade and emissions scenario currently selected on the map. Hover over values to see the likely range (10th to 90th percentile) for any given value. Projected decreases are denoted by a minus (-) sign.

		Nashua Basin				
		Projected change in Average Temperature (°F)				
Season	Baseline (°F)	Emissions Scenario	2030s	2050s	2070s	2090s
Annual	46.77	High RCP8.5	+3.66	+5.44	+7.54	+9.36
		Medium RCP4.5	+2.86	+4.05	+4.79	+5.12
Fall	49.01	High RCP8.5	+3.92	+5.71	+8.62	+10.24
		Medium RCP4.5	+3.19	+4.23	+4.78	+5.17
Spring	44.94	High RCP8.5	+3.01	+4.74	+6.65	+8.13
		Medium RCP4.5	+2.53	+3.24	+4.28	+5.13
Summer	67.56	High RCP8.5	+3.98	+5.95	+8.44	+10.61
		Medium RCP4.5	+2.98	+4.26	+4.6	+5.03
Winter	25.20	High RCP8.5	+3.68	+5.4	+7.59	+9.31
		Medium RCP4.5	+3.14	+4.41	+5.13	+5.09

Major Basins NASHUA

Figure 15. Projected warming for the Nashua River Basin by target decade, as available on ResilientMA.

RCP 4.5



RCP 8.5

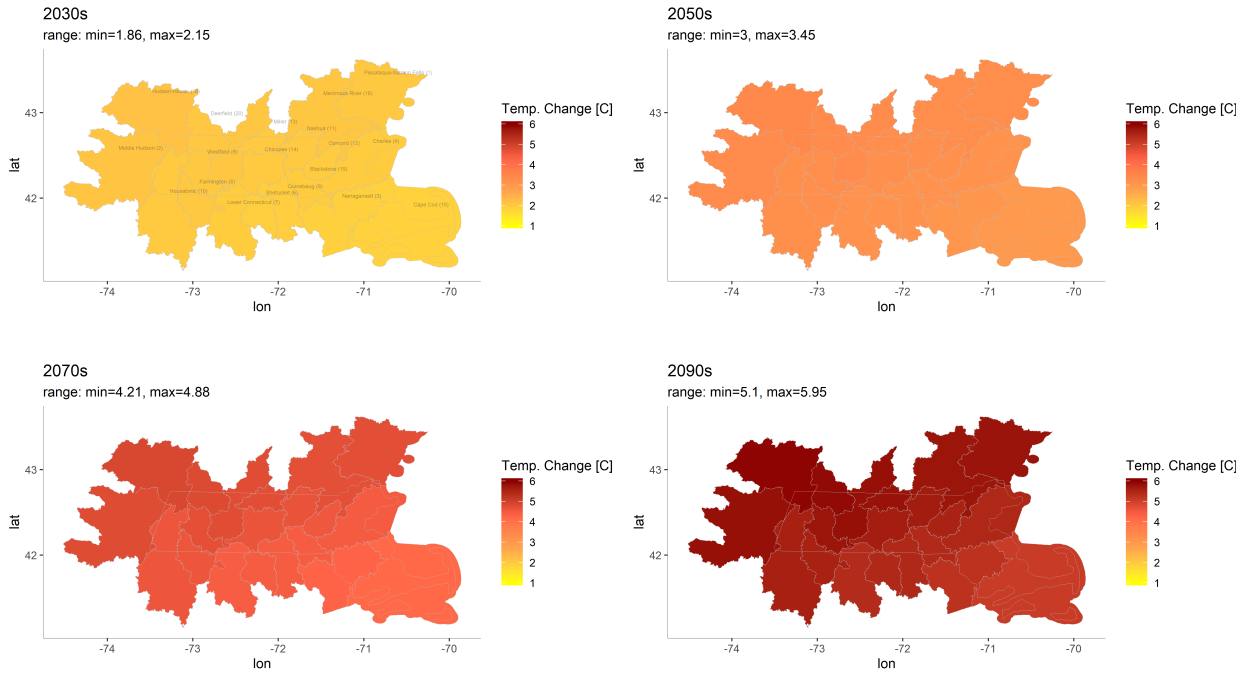


Figure 16. Projected warming in 2030s, 2050s, 2070s, and 2090s for 20 basins across the state of Massachusetts based on MACA downscaled data for RCP 4.5 and RCP 8.5. The minimum and maximum projected average annual temperature change [°C] are also provided.

7. Conclusion

This report presents an analysis of extreme precipitation scaling with dew point temperature, both in observations across the Northeast United States and for a subset of downscaled CMIP5 projections within the state of Massachusetts. Our scaling analysis is novel in comparison with past work based on a comparative analysis of scaling at annual, seasonal, and daily scales; diagnostics to better understand the spatial and temporal linkages between dew point temperatures and extreme precipitation; the use of hierarchical Bayesian models to more accurately estimate scaling rates through partial pooling of data across sites; and the examination of scaling rates across different weather regimes that influence the Northeast US.

The primary conclusions of this report are that empirical scaling rates of extreme precipitation with warming range between 0% and 11% per °C, with average scaling rates across seasons and methods ranging between 3% and 5% per °C. To implement these scaling rates for stakeholder use, this report recommends scaling design storms at sub-daily to daily time scales from the NOAA Atlas 14 product at the theoretical rate of 7% per °C. A database of updated IDF curves has been developed across the state of Massachusetts for different temperature changes based on this scaling rate. Based on the target decade of interest and the associated warming for that decade from an ensemble of GCM projections, new climate-change informed IDF curves can be retrieved for any location in the state.

The conclusions of this report should be interpreted in the context of the limitations of this study. First, many of the gauges used in the observational analysis were limited in their record length due to the paucity of long-term gauges with measurements of dew point temperature. This limited record significantly increases the uncertainty in model parameter estimates (and thus the scaling rates). While hierarchical Bayesian models were forwarded to partially pool information across sites and reduce some of this uncertainty, it cannot be eliminated. Furthermore, all inferences were based on empirical scaling rates for daily data, but recommendations were extended to sub-daily scales to support complete IDF curve updates. While a margin of safety was included in the recommended scaling, further analysis should be conducted to confirm appropriate scaling rates for sub-daily timescales.

The analysis of scaling rates within the climate models is accompanied by all of the caveats that come with using downscaled climate model data. It is not clear whether the mechanisms that drive extreme precipitation across seasons are well reproduced in the climate models, nor is it clear whether the downscaling and bias correction techniques used to process climate model output imposed statistical artifacts in the data that would influence estimated scaling rates. Finally, the changes to extreme precipitation suggested by scaling rates with dew point temperature only reflect thermodynamic shifts to daily extreme precipitation, and ignore possible changes to extreme precipitation rates to changes in the frequency or trajectories of storm tracks. These latter changes, though highly uncertain, could have significant impacts on the actual extreme precipitation events experienced in the future under climate change.

Acknowledgements

This work was supported by the Massachusetts Executive Office of Energy and Environmental Affairs.

References

- Abatzoglou, J. T. (2013). Development of gridded surface meteorological data for ecological applications and modelling. *Int. J. Climatol.*, 33, 121–131.
- Abatzoglou, J.T., and Brown, T.J. (2012). A comparison of statistical downscaling methods suited for wildfire applications. *International Journal of Climatology*, 32, 772–780.
- Alduchov, O. A., & Eskridge, R. E. (1996). Improved Magnus form approximation of saturation vapor pressure. *Journal of applied meteorology*, 35(4), 601–609.
- Ali, H., Fowler, H. J., & Mishra, V. (2018). Global observational evidence of strong linkage between dew point temperature and precipitation extremes. *Geophysical Research Letters*, 45(22), 12–320.
- Allan, R. P., & Soden, B. J. (2008). Atmospheric warming and the amplification of precipitation extremes. *Science*, 321(5895), 1481–1484.
- Allen, M. R., & Ingram, W. J. (2002). Constraints on future changes in climate and the hydrologic cycle. *Nature*, 419(6903), 228–232.
- Barnes, E.A. and L. Polvani (2013), Response of the Midlatitude Jets, and of Their Variability, to Increased Greenhouse Gases in the CMIP5 Models, *J. Climate*, 26, 7117–7135, <https://doi.org/10.1175/JCLI-D-12-00536.1>.
- Coles, S., Bawa, J., Trenner, L., & Dorazio, P. (2001). *An introduction to statistical modeling of extreme values* (Vol. 208, p. 208). London: Springer.
- DeGaetano, A. T., and C. M. Castellano (2017). Future projections of extreme precipitation intensity-duration-frequency curves for climate adaptation planning in New York State. *Climate Services*, 5, 23–35, <https://doi.org/10.1016/j.cliser.2017.03.003>.
- Deser, C., Phillips, A., Bourdette, V. et al. (2012), Uncertainty in climate change projections: the role of internal variability, *Clim Dyn*, 38: 527. <https://doi.org/10.1007/s00382-010-0977-x>
- Duane, S., Kennedy, A. D., Pendleton, B. J., and Roweth D. (1987). Hybrid Monte Carlo, *Phys. Lett. B*, 195(2), 216–222.
- Emori, S., and Brown, S.J. (2005), Dynamic and thermodynamic changes in mean and extreme precipitation under climate change, *Geophysical Research Letters*, 32 (17), L17706, doi:10.1029/2005GL023272.
- Gelman, A., and Rubin, D.B. (1992). Inference from iterative simulation using multiple sequences, *Stat. Sci.*, 7(4), 457–511.
- Gittleman, J. L., & Kot, M. (1990). Adaptation: statistics and a null model for estimating phylogenetic effects. *Systematic Zoology*, 39(3), 227–241.
- Han, W., J. Vialard, M.J. McPhaden, T. Lee, Y. Masumoto, M. Feng, and W.P. de Ruijter (2014), Indian Ocean Decadal Variability: A Review. *Bull. Amer. Meteor. Soc.*, 95, 1679–1703, <https://doi.org/10.1175/BAMS-D-13-00028.1>
- Hawcroft, M.K., Shaffrey, L.C., Hodges, K.I., Dacre, H.F. (2016), Can climate models represent the precipitation associated with extratropical cyclones, *Clim Dyn*, 47, 679–695. <https://doi.org/10.1007/s00382-015-2863-z>
- Hawkins, E., and Sutton, R. (2011). The potential to narrow uncertainty in projections of regional precipitation change. *Clim Dyn.*, 37(1–2), 407–418.
- Howarth, M. E., Thorncroft, C. D., & Bosart, L. F. (2019). Changes in Extreme Precipitation in the Northeast United States: 1979–2014, *Journal of Hydrometeorology*, 20(4), 673–689.
- IPCC (2013), *Climate Change 2013: The Physical Science Basis. Contribution of Working Group I to the Fifth Assessment Report of the Intergovernmental Panel on Climate Change* [Stocker, T.F., D. Qin, G.-K. Plattner, M. Tignor, S.K. Allen, J. Boschung, A.

- Nauels, Y. Xia, V. Bex and P.M. Midgley (eds.)]. Cambridge University Press, Cambridge, United Kingdom and New York, NY, USA, 1535 pp.
- Jones, C., Giorgi, F., and Asrar, G. (2011). The Coordinated Downscaling Experiment: CORDEX; an international downscaling link to CMIP5. *CLIVAR Exch.*, 16, 34–40.
- Kalnay, et al. (1996). The NCEP/NCAR 40-year reanalysis project. *Bulletin of the American meteorological Society*, 77(3), 437–472.
- Knutti, R. & Sedlacek, J. (2013), Robustness and uncertainties in the new CMIP5 climate model projections. *Nature Clim. Change* 3, 369–373.
- Knutti, R., D. Masson, and A. Gettelman (2013), Climate model genealogy: Generation CMIP5 and how we got there, *Geophys. Res. Lett.*, 40, 1194–1199, doi:10.1002/grl.50256.
- Koenker, R., & Machado, J. A. (1999). Goodness of fit and related inference processes for quantile regression. *Journal of the American Statistical Association*, (448), 1296–1310.
- Lawrence, M. G. (2005). The relationship between relative humidity and the dewpoint temperature in moist air: A simple conversion and applications. *Bull. Amer. Meteor. Soc.*, 86, 225-233. doi: <http://dx.doi.org/10.1175/BAMS-86-2-225>
- Lenderink, G., Barbero, R., Loriaux, J. M., & Fowler, H. J. (2017). Super-Clausius–Clapeyron Scaling of Extreme Hourly Convective Precipitation and Its Relation to Large-Scale Atmospheric Conditions, *Journal of Climate*, 30(15), 6037-6052.
- Liu, Z. (2012), Dynamics of Interdecadal Climate Variability: A Historical Perspective. *J. Climate*, 25, 1963–1995, <https://doi.org/10.1175/2011JCLI3980.1>
- Livneh, B., T. J. Bohn, D. W. Pierce, F. Munoz-Arriola, B. Nijssen, R. Vose, D. R. Cayan, and L. Brekke, (2015). A spatially comprehensive, hydrometeorological data set for Mexico, the U.S., and Southern Canada 1950-2013. *Scientific Data*, v. 2, article 150042 (2015). doi:10.1038/sdata.2015.42.
- Lopez-Cantu, T., Prein, A. F., & Samaras, C. (2020). Uncertainties in future U.S. extreme precipitation from downscaled climate projections. *Geophysical Research Letters*, 47, e2019GL086797. <https://doi.org/10.1029/2019GL086797>
- Magan, B., Kim, S., Wasko, C., Barbero, R., Moron, V., Nathan, R., & Sharma, A. (2020). Impact of atmospheric circulation on the rainfall-temperature relationship in Australia. *Environmental Research Letters*, 15(9), 094098.
- Maraun, D., et al. (2017), Towards process-informed bias correction of climate change simulations. *Nat. Climate Change*, 7, 764–773, <https://doi.org/10.1038/nclimate3418>.
- Martinkova, M., & Kysely, J. (2020). Overview of observed Clausius-Clapeyron scaling of extreme precipitation in midlatitudes. *Atmosphere*, 11(8), 786.
- Molnar, P., Fatichi, S., Gaál, L., Szolgay, J., and Burlando, P.: Storm type effects on super Clausius–Clapeyron scaling of intense rainstorm properties with air temperature, *Hydrol. Earth Syst. Sci.*, 19, 1753–1766, <https://doi.org/10.5194/hess-19-1753-2015>, 2015.
- Moran, P. A. (1950). Notes on continuous stochastic phenomena. *Biometrika*, 37(1/2), 17-23.
- Newman, M., M.A. Alexander, T.R. Ault, K.M. Cobb, C. Deser, E. Di Lorenzo, N.J. Mantua, A.J. Miller, S. Minobe, H. Nakamura, N. Schneider, D.J. Vimont, A.S. Phillips, J.D. Scott, and C.A. Smith (2016), The Pacific Decadal Oscillation, Revisited, *J. Climate*, 29, 4399–4427, <https://doi.org/10.1175/JCLI-D-15-0508.1>
- Park, I., & Min, S. (2017). Role of Convective Precipitation in the Relationship between Subdaily Extreme Precipitation and Temperature, *Journal of Climate*, 30(23), 9527-9537.
- Perica, S., Pavlovic, S., St. Laurent, M., Trypaluk, C., Unruh, D., Martin, D., Wilhite, O. (2015, revised 2019). NOAA Atlas 14 Volume 10 Version 3, Precipitation-Frequency Atlas of

- the United States, Northeastern States. NOAA, National Weather Service, Silver Spring, MD.
- Pfahl S., O’Gorman, P.A., Fischer, E.M. (2017), Understanding the regional pattern of projected future changes in extreme precipitation, *Nature Climate Change*, 7 (6), 423-427.
- Pierce, D.W., Cayan, D. R., and Thrasher, B. L. (2014). Statistical downscaling using localized constructed analogs (LOCA). *J. Hydrometeor.*,15, 2558–2585, <https://doi.org/10.1175/JHM-D-14-0082.1>.
- Plummer, M., et al. (2003). Jags: A program for analysis of bayesian graphical models using gibbs sampling. In *Proceedings of the 3rd international workshop on distributed statistical computing* (Vol. 124).
- Pumo, D., Carlino, G., Blenkinsop, S., Arnone, E., Fowler, H., & Noto, L. V. (2019). Sensitivity of extreme rainfall to temperature in semi-arid mediterranean regions. *Atmospheric Research*, 225, 30–44.
- Randall, D., M. Khairoutdinov, A. Arakawa, and W. Grabowski (2003), Breaking the Cloud Parameterization Deadlock. *Bull. Amer. Meteor. Soc.*, 84, 1547–1564, <https://doi.org/10.1175/BAMS-84-11-1547>
- Schroeder, K., Kirchengast, G. Sensitivity of extreme precipitation to temperature: the variability of scaling factors from a regional to local perspective. *Clim Dyn* 50, 3981–3994 (2018). <https://doi.org/10.1007/s00382-017-3857-9>
- Seager, R., Naik, N., and Vecchi, G.A. (2010), Thermodynamic and dynamic mechanisms for large-scale changes in the hydrologic cycle in response to global warming, *Journal of Climate*, 23 (17), 4651-4668.
- Shepherd (2014), Atmospheric circulation as a source of uncertainty in climate change projections, *Nature Geosciences*, 7 (10), 703-708.
- Steinschneider, S., R. McCrary, L. O. Mearns, and C. Brown (2015), The effects of climate model similarity on probabilistic climate projections and the implications for local, risk-based adaptation planning. *Geophys. Res. Lett.*, 42, 5014–5044. doi: 10.1002/2015GL064529.
- Thibeault, J. M., and A. Seth (2015), Toward the credibility of northeast United States summer precipitation projections in CMIP5 and NARCCAP simulations, *J. Geophys. Res. Atmos.*, 120, 10050–10073, doi:10.1002/2015JD023177.
- van Niekerk, A., Scinocca, J. F. & Shepherd, T. G. (2017), The modulation of stationary waves, and their response to climate change, by parameterized orographic drag, *J. Atmos. Sci.* 74, 2557–2574.
- Visser, J., Wasko, C., Sharma, A., & Nathan, R. (2020). Resolving inconsistencies in extreme precipitation-temperature sensitivities. *Geophysical Research Letters*, 47(18), e2020GL089723
- Wang, G., Kirchoff, C. J., Seth, A., Abatzoglou, J. T., Livneh, B., Pierce, D. W., Fomenko, L., & Ding, T. (2020). Projected Changes of Precipitation Characteristics Depend on Downscaling Method and Training Data: MACA versus LOCA Using the U.S. Northeast as an Example, *Journal of Hydrometeorology*, 21(12), 2739-2758
- Woollings, T. (2010), Dynamical influences on European climate: an uncertain future. *Phil. Trans. R. Soc. A* 368, 3733–3756.
- Yu, K., & Moyeed, R. A. (2001). Bayesian quantile regression. *Statistics & Probability Letters*,54(4), 437–447.

- Yu, K., & Zhang, J.(2005). A three-parameter asymmetric Laplace distribution and its extension. *Communications in Statistics—Theory and Methods*, 34(9-10),1867–1879
- Zappa, G., Shaffrey, L. C. &Hodges, K. I. (2013), The ability of CMIP5 models to simulate North Atlantic extratropical cyclones. *J. Clim.* 26, 5379–5396.
- Zhang, X., Zwiers, F. W., Li, G., Wan, H., & Cannon, A. J. (2017). Complexity in estimating past and future extreme short-duration rainfall. *Nature Geoscience*, 10(4), 255– 259.